# The GLM-Spectrum: A multilevel framework for spectrum analysis with covariate and confound modelling.

Andrew J Quinn[1, 2†], Lauren Atkinson [1], Chetan Gohil [1], Oliver Kohl [1], Jemma Pitt [1], Catharina Zich [3, 4], Anna C Nobre [1, 5] & Mark W Woolrich[1]

**1** Oxford Centre for Human Brain Activity, Wellcome Centre for Integrative Neuroimaging, University Department of Psychiatry, Warneford Hospital, Oxford, UK.
**2** Centre for Human Brain Health, School of Psychology, University of Birmingham, UK.
**3** Department for Clinical and Movement Neurosciences, UCL Queen Square Institute of Neurology, 33 Queen Square, London, UK
**4** FMRIB, Wellcome Centre for Integrative Neuroimaging, Nuffield Department of Clinical Neurosciences, University of Oxford, UK.
**5** Department of Experimental Psychology, University of Oxford, UK

† corresponding author: a.quinn@bham.ac.uk

## Abstract

Spectrum estimators that make use of averaging across time segments are ubiquitous across neuroscience. The core of this approach has not changed substantially since the 1960s, though many advances in the field of regression modelling and statistics have been made during this time. Here, we propose a new approach, the General Linear Model (GLM) Spectrum, which reframes time averaged spectral estimation as multiple regression. This brings several benefits, including the ability to do confound modelling, hierarchical modelling and significance testing via non-parametric statistics.

We apply the approach to a first-level EEG resting-state dataset alternating between eyes open and eyes closed resting-state. The GLM-Spectrum can model both conditions, quantify their differences, and perform denoising through confound regression in a single step. This application is scaled up from a single channel to a whole-head recording and, finally, applied to quantify age differences across a large group-level dataset. We show that the GLM-Spectrum lends itself to rigorous modelling of within- and between-subject contrasts as well as their interactions, and that the use of model-projected spectra provides an intuitive visualisation. The GLM-Spectrum is a flexible framework for robust multi-level analysis of power spectra, with adaptive covariance and confound modelling.

# 1 Introduction

Frequency-domain analyses of oscillations in electrophysiological recordings of brain activity contain information about the underlying neuronal activity. Both the peaks of specific oscillations and the broader spectral shape are informative about brain function and have inspired a wide literature (Buzsáki and Draguhn, 2004; Kopell et al., 2014). The windowed periodogram is the predominant method for spectrum estimation in neuroscience. It computes the average Fourier spectrum across a set of sliding window segments (Bartlett, 1948, 1950; Welch, 1967) based on the premise that the data are comparable over time and that the effect of noise will be attenuated when averaging across segments. This algorithm produces a statistical estimate of a spectrum and has remained largely the same for many decades. Statistical methods have greatly progressed in this time and many newer approaches can be directly applied to the windowed periodogram.

Here, we propose the General Linear Model Spectrum (GLM-Spectrum) framework for analysing Fourier spectra. This reframes the method of averaged periodograms as a regression problem by modelling frequency spectra over successive windows as a linear mixture of a set of user-specified regressors. This links linear spectrum estimation to the GLM analyses that have been developed for a broad range of neuroimaging applications including structural and functional MRI (Friston et al., 1994; Woolrich et al., 2009), event related fields (Smith and Kutas, 2014) and induced responses (Litvak et al., 2013). Specifically, we apply a General Linear Modelling approach to frequency spectrum estimation and demonstrate the utility of multi-level models (Friston, 2007; Woolrich et al., 2004), non-parametric permutation testing (Nichols and Holmes, 2001; Winkler et al., 2014), contrast coding and confound regression in this context.

We illustrate the utility and flexibility of the GLM-Spectrum by analysing EEG recordings alternating between eyes open and eyes closed resting-state conditions from a freely available dataset (Babayan et al., 2019). First, the GLM-Spectrum is illustrated in detail with data from a single channel of one individual. The spectrum for the two resting conditions and their difference are computed, whilst a set of covariate and confound regressors account for linear trends over time and a diverse set of potential artefact sources. This approach is generalised to the whole-head recording of a single subject to describe the spatial patterns associated with each regressor. Finally, a group-level, whole-head analysis explores the GLM-Spectra of specific regressors and contrasts before quantifying how they differ between younger and older participants.

# 2 Methods

## 2.1 Time-Averaged Periodogram Estimation

We start by reviewing the definition of the established method for windowed periodogram estimation. The discrete Fourier transform (DFT) can be used to map a series of data points from the time domain into the frequency domain. The frequency domain representation is known as a spectrum and describes how the variance in the data is distributed across frequencies according to a linear basis set. The DFT computes the frequency spectrum $Y(f)$ from an input time series of real values at discrete time points $y(t)$.

$$Y(f) = \sum_{t=0}^{N-1} y(t) e^{\frac{-i2\pi ft}{fs}} \tag{1}$$

Where $t$ is a discrete time point, $f$ is a discrete frequency, $fs$ is the sampling frequency in Hz and $N$ is the number of data points. The output, $Y(f)$, is a complex-valued array containing the estimate of the spectrum. In practice, the computationally efficient Fast Fourier Transform (FFT; Cooley and Tukey (1965)) implementation of the DFT is applied by most software packages. We will use the FFT for this section, as it refers to the algorithm that is most commonly used in practice.

The mathematics underlying the FFT works with an infinite time series. However, the data from real measurements are finite. Therefore, the FFT must implicitly assume that the time-limited input data, $y(t)$, repeats infinitely many times. The combination of this repetition and the discrete sampling of the time-series $y(t)$ leads to the frequency output of the FFT being a linearly spaced axis of N frequency values spanning between $-\frac{fs}{2}$ to $+\frac{fs}{2}$. In addition, the discontinuities between repetitions lead to an effect known as spectral leakage, which spreads power contained in one frequency bin to its neighbours. Finally, the computational efficiency of the FFT relies on the input data length $N$ being an integer power of 2. If it is not, then the routine will zero-pad the length of the input up to a power of 2. This padding causes further sharp changes and discontinuities that can lead to spectral leakage.

The impact of the spectral leakage is reduced by applying a tapered window function designed to flatten the data at the start and end of each segment to minimise discontinuities between repetitions. Here, we modify equation 1 to multiply a window function $w(t)$ with the data (point-by-point) during the FFT:

$$Y(f) = \sum_{t=0}^{N-1} w(t) y(t) e^{\frac{-i2\pi ft}{fs}} \tag{2}$$

There is a huge range of possible window functions that provide different profiles of spectral leakage and sensitivity. The Hamming and Hann windows (used by MatLab's 'pwelch' function[1] and SciPy's 'scipy.signal.welch' function [2], respectively) are two commonly applied options which offer reasonable narrowband resolution. More advanced tapering can be applied using discrete prolate spheroid sequences (DPSS) to create a Multi-Tapered Spectrum estimate (Prerau et al., 2017; Thomson, 1982).

Y(f) is complex-valued, with its real and imaginary parts reflecting the sine and cosine components of the Fourier transform. The phase and magnitude of each

[1] `https://www.mathworks.com/help/signal/ref/pwelch.html`
[2] `https://docs.scipy.org/doc/scipy/reference/generated/scipy.signal.welch.html`

frequency component can be computed from these complex values, though spectrum analyses most commonly use the magnitude. We can take the absolute value of $Y(f)$ to create a *magnitude spectrum* $S_y(f)$.

$$S_y(f) = |Y(f)| \tag{3}$$

Similarly, a power spectral density (sometimes just called a power spectrum) can be calculated by taking the squared absolute value normalised by the data length:

$$P_y(f) = \frac{|Y(f)|^2}{N} \tag{4}$$

$P_y(f)$ is a real-valued estimate of the spectral density of a signal, sometimes known as a periodogram. This periodogram provides a relatively simple spectrum estimation but has a further shortcoming. Only one estimate for the power at each frequency is calculated, irrespective of the length of $y(t)$. This means that we have no information about the variance around that estimate, and the estimate does not improve if we include more data.

A better estimator is the Time-Averaged Periodogram (TAP), introduced by Maurice Bartlett (Bartlett, 1948, 1950) and refined by Peter Welch (Welch, 1967). These methods are commonly used and ensure that the noise level in the periodogram reduces as the length of the input data increases by a method of ensemble averaging (at the expense of information about low frequencies). This splits the input into a set of $k = 1, 2, \ldots K$ segments (i.e., time windows) each containing $t = 1, 2, \ldots T$ samples and computes the FFT of each to produce a short time Fourier transform (STFT):

$$S_y(f, k) = \sum_{t=1}^{T} w(t) y(t, k) e^{\frac{-i2\pi ft}{fs}} \tag{5}$$

The input for each FFT is now the k-th segment of the continuous input $y(t)$, which we denote with $y(t, k)$. The output matrix $Y(f, k)$ contains the STFT, which describes how the spectrum changes in power across the $K$ segments. A time-varying magnitude spectrum can be computed by taking the absolute value of the STFT.

$$S_y(f, k) = |Y(f, k)| \tag{6}$$

Similarly, a time-varying power spectral density is computed from the squared absolute of the STFT.

$$P_y(f, k) = \frac{|Y(f, k)|^2}{N} \tag{7}$$

Finally, the TAP is then the average of the time-varying power spectral density across segments. If the previous computations included the windowing function $w(t)$ and overlapping time segments, then this is Welch's power spectral density estimate (Welch, 1967).

$$Pwelch_y(f) = \frac{1}{K}\sum_{k=1}^{K} P_y(f,k) \tag{8}$$

Welch's TAP now has the property that the noise level of the estimate decreases with increased data length, since more input data provides a larger number of segments for the central averaging step. It is still an imperfect estimator that has been subject to criticism (Prerau et al., 2017; Thomson, 1982) but it is practical, straightforward to compute, and in wide use across science and engineering.

The real-valued power spectrum may additionally be scaled by a log-transform to produce a log-power spectrum $log(P_y(f,k))$. This can be desirable as the power spectrum is strictly positive and tends to have a strongly non-Gaussian distribution, whereas the log-power spectrum is not strictly positive and tends to have a more Gaussian distribution (See supplemental section 7.1).

Several key parameters must be set by the user when computing a spectrum in this way. These values affect the range and resolution of the spectrum and must be chosen with care. Briefly, there are three main considerations. Firstly, longer segment lengths ($T$) will increase the frequency resolution (number of bins per Hertz). Secondly, faster data sampling rates allows higher frequencies to be estimated (by increasing the Nyquist range). Finally, increasing the length of the input time-series for a given segment length will increase the number of segments in the average, reducing the impact of noise. These choices are discussed in full in Supplemental section 7.2.

## 2.2 General Linear Model Spectrum

The GLM-Spectrum replaces the averaging step in the time-averaged spectrum estimation methods with a General Linear Model (also known as multiple regression). The GLM is widely used in neuroimaging analyses (Friston, 2007; Woolrich et al., 2009) and the same principles around analysis, model validation and statistics apply here. The objective is to model the spectrum across the K sliding window segments as a linear function of a set of regressor variables. The magnitude GLM-Spectrum is defined as:

$$S_y(f,k) = X(k)B(f) + e(f) \tag{9}$$

Where $S_y(f)$ is the (Kx1) time-varying spectrum estimated at frequency ($f$) across all $K$ segments/windows (the STFT computed in 6) computed from a single channel (timeseries) of data, X is a (KxP) design matrix containing the P regressors of interest as they vary over time, and e(f) is a (Kx1) vector of residual errors. We model the whole spectrum using a mass-univariate modelling approach that fits a separate GLM for each frequency bin in the FFT. The resulting (Px1) vector B(f) contains the estimated regression parameters. We refer to the whole vector of estimates across frequency as the GLM 'beta-spectrum'.

We assume that the data being modelled (the dependant variable) follows a normal, Gaussian distribution and that the residuals $e(f)$ are Gaussian, independent and identically distributed (IID) over time, i.e. k. Violations of these assumptions will be discussed later in section 2.4.

A critical choice is which form of the time-varying spectrum to use as the dependant variable; the complex, magnitude, power and log-power spectra are linked by non-linear transforms and have very different distributions. The power spectrum is typically strongly non-Gaussian and will need to be transformed prior to modelling.

The magnitude and log-power spectra are more likely to have a Gaussian spectrum. We typically will not model the complex spectrum as any phase differences across windows could lead to structure being averaged out of the final spectrum. If phase information is critical, and expected to be consistent across time-segments, then future work may generalise these statistics to the complex spectrum (for example, Baker (2021)).

Here, we will focus on modelling the magnitude spectrum, which works well for the specific data used here (see supplemental section 7.1). In future, the GLM-Spectrum approach could be extended to use Generalised Linear Modelling (Nelder and Wedderburn, 1972) to account for specific differences in the distribution of the data being modelled.

## 2.3 Estimating the GLM Parameters

Once the design matrix has been specified and the data have been transformed into the STFT, we are ready to fit the regression parameters B in equation 9. Under the assumptions specified above, this can be achieved using Ordinary Least Squares (OLS) to estimate the regression parameters (also known as beta-estimates), $B(f)$, as

$$\hat{B}(f) = (X^T X)^{-1} X^T S_y(f) \tag{10}$$

Alternatively, we can pre-multiply the data by the Moore-Penrose pseudo-inverse (Penrose, 1956) of the design matrix, which performs well even when there are multi-collinearities in $X$ (see Section 2.4):

$$\hat{B}(f) = X^+ S_y(f) \tag{11}$$

Where the superscript $^+$ denotes the Moore-Penrose pseudo-inverse. More complex fitting routines could be used if the assumptions underlying OLS are inappropriate for a particular application. For example, the rest of the GLM-Spectrum framework would work in the same way if $B(f)$ were estimated using a robust or regularised regression. Similarly, it would be possible to extend the approach to Bayesian regression methods. Here, we use the pseudo-inverse model fitting approach (equation 11) for all GLM estimation.

## 2.4 Assumptions of the GLM-Spectrum model

A statistical model such as the GLM is only valid if its assumptions are met. These critical assumptions must be checked to ensure the validity of the GLM model fit (Monti, 2011). We highlight three cases here. Firstly, the distribution of the spectrum data to be fitted should be assessed prior to the application of the GLM-Spectrum as highlighted in section 2.2. Secondly, the values in the error term $e(f)$ must be Gaussian distributed and finally the values in the error term $e(f)$ must be independently and identically distributed (IID).

The presence of any temporal autocorrelation in $e(f)$ indicates a violation of the second assumption. This issue is commonly encountered in other time-series models such as first-level fMRI analyses (Friston et al., 2000; Woolrich et al., 2001; Worsley and Friston, 1995) and is a strong concern for first-level GLM-Spectra. Many time-averaged periodogram implementations are computed from overlapping data segments that are not independent of their neighbours. Care must be taken to specify STFT parameters that maximise the independence of each data segment, particularly if first-level permutation statistics are of interest. We recommend inspecting the model residuals for

temporal autocorrelation using a metric such as the Durbin-Watson statistic (Durbin and Watson, 1950, 1951) (see supplemental section 7.3). If this condition is not met, then the estimates of the GLM-Spectra (i.e. the regression parameter estimates can still be used, but any first-level statistics do not reflect an inferential statistic and must be taken as purely descriptive results. It should be noted that this allows subsequent group analyses to be carried out, as these depend on the GLM-Spectra estimates and not on their statistics. Future work may develop explicit models for this temporal autocorrelation similar to those used in fMRI to make statistics on individual session estimates of the GLM-Spectra valid (Friston et al., 2000; Woolrich et al., 2001).

Finally, while it is not a violation of the model assumptions, one should take care when regressors in X can be expressed, to any extent, as a linear combination of other regressors. This is called multicollinearity in the GLM literature and means that there are infinite equally good solutions to the regression equation. The Moore-Penrose pseudo-inverse (MPPI) can overcome this limitation. If multiple solutions to equation 9 exist, the MPPI will return the regression parameters with the minimum Euclidean norm (Penrose, 1956). Note that when there is partial multicollinearity, the MPPI uses the component of the regressor that is uncorrelated with the rest of the design matrix (i.e. corresponding to any unique variability in that regressor) to find each parameter estimate. This property means the MPPI solution quantifies the unique effect of each regressor that cannot be accounted for by the others. Therefore, it is frequently desirable to proceed with the MPPI solution for a GLM whose design contains some degree of multicollinearity that we wish to eliminate from the results.

In addition, the impact of any multicollinearity is naturally accounted for in the variance of the affected regression parameter estimates; for example, when it is not clear what a regression parameter's value should be due to multicollinearity, then that parameter estimate's variance (as computed in section 2.5) will be appropriately increased. Nonetheless, even when using the MPPI, we recommend assessing the correlation and singular value spectrum of the design matrix prior to model fitting as well as the variance of the regression parameters (Smith et al., 2007), to ensure that one is aware of the potential impact of multicollinearity on finding a significant result. If these checks identify unexplainable or unintended multicollinearity, perhaps from inclusion of too many or inappropriate regressors, then the design should be re-assessed prior to further analysis.

## 2.5 Contrasts and t-statistics

Once the design matrix is specified and the model parameters have been estimated, the GLM-Spectrum consists of a beta-spectrum for each regressor. This beta-spectrum contains the regression parameter estimates quantifying the linear effect of that regressor across the frequency range.

Next, we can compute simple linear combinations of regression parameter estimates, known as contrasts. Contrasts can be defined to ask questions about the size of these linear combinations, including whether they are significantly different to zero (using t-tests). This approach is commonly applied in neuroimaging applications (Friston, 2007; Woolrich et al., 2009).

Each contrast is defined as a vector of values defining the relative weightings between the regression parameter estimates of the regressors. For example, we could define the following contrasts for a model that contains three regressors in its design matrix:

$$c_1 = \begin{bmatrix} 1 \\ 0 \\ 0 \end{bmatrix}, c_2 = \begin{bmatrix} 0 \\ 0.5 \\ 0.5 \end{bmatrix}, c_3 = \begin{bmatrix} 0 \\ 1 \\ -1 \end{bmatrix}, C = [c_1, c_2, c_3] \tag{12}$$

Where C is a (P x $N_c$) matrix containing all $N_c$ contrasts. Using terminology common in neuroimaging, these contrasts define a Contrast Of Parameter Estimates, or a cope, which is computed from a matrix multiplication between the contrast and the model parameter estimates:

$$cope(f) = C\hat{B}(f) \tag{13}$$

Here, we refer to the resulting frequency resolved vector of cope values, cope(f), as the GLM cope-spectrum. The individual contrasts are designed to ask specific experimental questions. Using the examples in equation 12, the first contrast asks whether $c_1\hat{B}(f) = 0$. This specifies a t-test that tests whether each value in beta-spectrum of the first regressor is different from zero; regressors two and three are weighted to zero in this specific contrast, but nevertheless still explain variance in the overall model. The second contrast tests if $c_2\hat{B}(f) = 0$ and asks whether the mean of the beta-spectra from regressors two and three is different from zero. Note that setting the values in this contrast to 0.5 that ensures that the contrast of the regression parameter estimates can be interpreted as the mean of the two regression parameters involved. When turned into statistics (see below), contrasts $c_1$ and $c_2$ are equivalent to one-sample t-tests in classical statistical frameworks.

Finally, testing if $c_3\hat{B}(f) = 0$ tests whether the difference in parameter estimates in the beta-spectrum of regressor 2 minus regressor 3 is different from zero. This will be equivalent to an independent samples t-test between the conditions modelled by these regressors. Regressor 1 is set to zero in the second two contrasts and is not directly included in the comparison. However, it is still explaining variance in the model and may be indirectly affecting the outcome of the contrast between regressors 2 and 3.

These contrasts are useful quantifications of different combinations of parameters estimates but we also need to compute the associated standard error to complete a formal statistical test. The ratio of the contrast value (cope) and its standard error is a t-statistic that indicates the estimated magnitude of a cope relative to its standard error. To compute the standard errors and subsequent t-statistics for each contrast, we first need to compute the residuals of the model fit:

$$R_y(f) = S_y(f) - \hat{B}(f)X \tag{14}$$

Note that $R_y(f)$ contains the actual set of residuals for a given dataset and model fit. This is distinct from $e_y(f)$, which denotes a more general white noise process. These residuals are used to compute the variance in the estimate of the cope, also known as a varcope. Firstly, we compute the variance of the residuals:

$$\sigma^2(f) = diag(R_y(f)R_y(f)^T) \tag{15}$$

And transform this to get the variance of relevant part of the model for this contrast:

$$varcope(f) = diag(C(X^TX)^{-1}C)\sigma^2(f) \tag{16}$$

$varcope(f)$ now contains the square of the standard error for this contrast. This computation can be costly with large datasets as several matrix multiplications must be performed. However, only the diagonal of the resultant matrix is used for further analysis. Therefore, we achieve a substantial speed-up in this computation using Einstein summation in numpy[3] to compute only the multiplications which appear in the final diagonal. More information on this is in Supplemental section 7.4. The spectrum of t-values corresponding to the contrast can then be computed as the ratio of the cope to its standard error:

$$t(f) = \frac{cope(f)}{\sqrt{varcope(f)}} \tag{17}$$

This GLM t-spectrum quantifies the difference of each cope from zero in statistical terms, incorporating both the parameter estimates and their standard errors. In practice, the varcope-spectrum values commonly scale linearly with the copes, leading to low t-values. This effect is commonly observed in neuroimaging data, particularly in fMRI. Here, we attenuate this effect by applying a median filter to smooth the varcope spectrum along the frequency dimension to compute a pseudo-t statistic, in combination with non-parametric permutations (see section 2.9; Nichols and Holmes (2001)). Further information on this is in supplemental section 7.5. Taken together, the GLM beta-spectrum $B(f)$, cope-spectrum $cope(f)$ and t-spectrum $t(f)$ provide an intuitive description of the frequency spectrum of the input data in terms of the specified regressors and contrasts.

## 2.6 Design Matrix Specification

The regressors in the design matrix $X$ will typically be secondary time-series that are recorded simultaneously with the main data or known *a priori*. The model tests for linear associations between these regressors and the spectrum estimates in the STFT. Therefore, the regressors must be prepared in the same manner as the main data, including any filtering and the segmentation, to ensure correspondence between the design matrix and data.

The GLM is a highly general method as the design matrix, $X$, can be adapted depending on the application in question. However, this flexibility can also make the specification and interpretation of the regressors challenging. The addition of a new regressor to an existing GLM design matrix can change the parameter estimates and standard errors of the previous regressors. Therefore, the final choice and interpretation of any regressors is necessarily specific to each individual analysis.

Standard time-averaged spectrum estimation methods (such as Welch's Periodogram) model the mean spectrum across time-segments. Similarly, most GLM-Spectrum analyses will also want to include regressors that quantify this average. In the simplest case, a single, constant regressor of ones is directly equivalent to the standard method. However, the flexibility of the GLM allows us to build on this and define more sophisticated models with multiple covariates if required.

One extension allowed by the GLM-Spectrum is to use confound regression to model the effect of an artefact source and attenuate its contribution to the estimate of the overall mean. Confound regression adaptively models the effect of the potential artefact each given dataset, only performing any denoising if a linear association between the confound regressor and the data can be identified. It is a flexible alternative to removing the artefact time periods altogether. Confound regression can

[3] `https://numpy.org/doc/stable/reference/generated/numpy.einsum.html`

be performed by including a non-zero mean regressor alongside a constant regressor in the design matrix. With this specification, the constant regressor models the intercept (the average where the value of the artefact regressor is zero) whilst the confound regressor quantifies the artefact effect. This example is explored in more detail in supplemental section 7.6.

Covariates can be included into the GLM in several ways. We can use indicator regressors (containing zeros and ones) which assume that the covariates effect will be the same each time it is present. Otherwise, we can use dynamic covariates to model phenomena that dynamically change over time in a continuous way. For example, this might include pupil-size, heart rate, or respiration rate. When we include these types of continuous regressors, their regression parameters capture the "slope" effect; in other words, how much does the spectrum change with each increment in the value of the regressor. For example, when including a pupil-size regressor, the spectrum resulting from its regression parameter estimates would indicate how much the power in a particular frequency bin increases or decreases as the pupil-size changes by a certain amount.

Another decision is whether to demean a given covariate regressor in the design matrix. Counter intuitively, the interpretation of the regression parameter estimate is unchanged when a covariate is demeaned; in both cases it is modelling the 'slope' effect that quantifies how much the spectrum changes with each increment of the regressor. In contrast, the interpretation of a constant regressor in the same model will change depending on whether a covariate is demeaned or not. A constant regressor will model the mean over all time points if the other covariates are demeaned and will model the intercept if non-zero mean regressors are included. As a result, confound regressors that are intended to remove a given effect from the estimate of the mean will typically have a non-zero mean whilst dynamic covariates that model changes around the mean will be demeaned or z-transformed prior to model fitting.

## 2.7 Model Projected Spectra

The GLM beta-, cope- and t-spectra assess parts of the overall time-varying spectrum in relation to the model. As these GLM-Spectra can relate to combinations of effects, their impact on the mean spectrum can be difficult to intuit. We propose computing the model-projected spectra to gain a more immediately intuitive visualisation of effects. This is a visualisation of how the spectrum changes for different value of the regressor of interest. For example, if the GLM-Spectrum of EEG data includes a covariate for pupil size then its beta-spectrum will describe how the spectrum changes as pupil size expands and contracts. The model-projected spectrum could then be used to visualise the predicted spectrum at a single, specific pupil size.

The model-projected spectrum is typically calculated for a descriptive range of values in the original regressor. In this paper, wee use the largest and smallest values from the regressor of interest. For example, to compute the projected spectrum for the largest and smallest value of a covariate regressor $Rv$ relative to a constant mean term, we use: model-projected spectra

$$max\{S_y|Rv\}(f) = max(Rv)\hat{B}_{rv}(f) + \hat{B}_{mean}(f) \tag{18}$$

$$min\{S_y|Rv\}(f) = min(Rv)\hat{B}_{rv}(f) + \hat{B}_{mean}(f) \tag{19}$$

$$\tag{20}$$

The max and min model-projected spectrum then describes the range of variability in the spectrum that is described by the regressor. Note that this is only a visualisation

method and that any apparent differences in these model projected spectra must be confirmed by statistical significance testing, such as non-parametric permutations (see section 2.9).

## 2.8 Group Models for GLM-Spectra

The GLM-Spectrum described thus far is used to describe continuous data recorded from a single session; we refer to this as the "first-level". We now consider how we can carry out a "group-level" analysis to combine the results across the first-level GLM-Spectra from multiple sessions/subjects using a group-level (or second-level) GLM (Beckmann et al., 2003; Friston et al., 2002; Woolrich et al., 2004). In brief, we create a group-level dependant variable by concatenating the parameter estimates, copes or varcopes from a set of first-level analyses and use another GLM to model how GLM-Spectra vary over sessions/subjects across the group. For example, here we fit a group-level beta-spectrum using the first-level cope-spectra for N subjects and a group-level design matrix:

$$\begin{bmatrix} cope^{j}_{subj1}(f) \\ cope^{j}_{subj2}(f) \\ \vdots \\ cope^{j}_{subjN}(f) \end{bmatrix} = X_{group}B_{group}(f) + e_{group}(f) \tag{21}$$

Where $cope^{j}_{subj1}(f)$ is the $j^{th}$ first-level cope computed for subject n at frequency bin , i.e. $cope^{j}_{subj1}(f) = c)j\hat{B}_{subjn}(f)$ where $c_j$ is the $j^{th}$ first-level contrast and $\hat{B}_{subjn}$ is the first-level contrast regression parameter estimates for subject $n$. Note that $X_{group}$ is the (NxQ) group-level design matrix and the (Qx1) matrix $B_{group}(f)$ is the group-level regression parameters, where Q is the number of group-level regressors. As with the first-level GLM, the error $e_{group}(f)$ is assumed to be Normal and IID.

As with the first-level analysis, the group-level GLM is fitted using OLS with the Moore-Penrose pseudo inverse; and is computed separately for each frequency, f, (and each channel or voxel – the indexing for which is not shown in the equations) in a mass-univariate manner. In addition, a separate group-level GLM is computed for each first-level cope of interest. As with the first-level GLM, contrasts can be used to ask a range of inference questions from the regression parameter estimates, $\hat{B}_{group}(f)$. A resource showing examples of commonly used group-level design matrices and contrasts is available online[4].

As shown in the equation above, the simplest group-level model carries forward the cope-spectra from a set of first-level analyses. This can be thought of as a fixed-effects group model in which each observation (first-level result) contributes equally to the group effect and the group-level GLM models the between-session/subject variability. This is the approach taken in this manuscript. This is straightforward to compute but neglects the information about the first-level standard errors in the varcope-spectra. This could be accounted for by carrying forward both the cope and varcope information to the group level and fitting a mixed effects model such as the FLAME method in fMRI (Woolrich et al., 2004). In practice, this model is challenging to fit as no simple closed-form estimation is available. Another alternative would be to carry the first-level t-statistics to the group level. Future work can explore wide range of possibilities for multi-level and mixed-modelling for the GLM-Spectrum.

[4] `https://fsl.fmrib.ox.ac.uk/fsl/fslwiki/GLM`

| Term | Definition |
|---|---|
| **STFT** | The short-time Fourier transform of a time series, containing the spectrum computed within sliding window time-segments across the data. Also called a time-varying spectrum. |
| **Design Matrix** | A matrix of regressors used to explain variability in observed data with a linear regression model. |
| **Regressor** | A single column of a design matrix containing explanatory variables relating to each individual observation. |
| **Beta-estimates** | A parameter estimate describing the linear relation between a regressor and the observed data. Also known as regression parameter estimates. |
| **Beta-Spectrum** | A vector of parameter estimates for a single regressor across the range of a frequency spectrum. |
| **Contrast** | A planned comparison between one or more parameter estimates. |
| **cope** | The result of a defined contrast between beta-estimates. |
| **cope-spectrum** | A vector of cope estimates for a single contrast across the range of a frequency spectrum. |
| **t-statistic** | The ratio of the departure of the estimated value of a contrast from its hypothesised value to its standard error. |
| **t-spectrum** | A vector of t-statistics for a single contrast across the range of a frequency spectrum. |
| **Model-Projected spectrum** | A visualisation of a spectrum as predicted by a fitted GLM set at a particular set of covariate values. |
| **First-Level GLM** | A linear model for a single data recording that models variability across time segments in a STFT with a specified design- and contrast-matrix resulting in a set of beta-, cope- and t-spectra. |
| **Group-Level GLM** | A linear model for a group dataset combining a set of first level GLM-Spectra. A group level design- and contrast-matrix models variability in first level beta or t-spectra across datasets resulting in a set of group-level beta-, cope- and t-spectra. |

**Table 1.** Glossary of definitions for the GLM-Spectrum.

## 2.9 Non-parametric Permutations

Null-hypothesis testing for a given contrast can be carried out with non-parametric permutations (Nichols and Holmes, 2001; Winkler et al., 2014). A null distribution of observed statistics is derived by recomputing the GLM after manipulating the design matrix in line with the null hypothesis. The observed group average is then compared to this null distribution and is 'significant' if it exceeds a pre-set critical threshold, such as the 95th percentile of the null distribution. Here, we perform non-parametric permutation testing to assess which frequencies and EEG sensors show significant group-level GLM effects.

Different forms of non-parametric permutation can be tailored to apply to for different hypothesis tests, though the overall procedure is similar for each. First, 'sign-flipping' permutations are used to test whether a test statistic significantly deviates from zero, or when the sum of the values in the contrast does not equal zero. Each row in the regressors of interest for this contrast have a 50% chance of being multiplied by minus one. This is under the null hypothesis that, if the observed statistic is not significantly different from zero then flipping the sign of the design matrix should not shift the mean. Second, 'row-shuffle' permutations are used for parametrically varying regressors. This scrambles the order of the rows in the regressor

at each permutation to test the null hypothesis that there is no correspondence between the regressor and observed data, so changing their order should not affect the test statistic. In all cases, we are only permuting the columns of the design matrix directly related to that contrast in question, whilst the remaining covariate structure of the design matrix stays unchanged.

Non-parametric permutation testing could, in principle, be carried out to assess the results of a first-level GLM-Spectrum. In contrast to a group-level analysis, the first level permutations would only assess whether a particular effect observed within a dataset could be expected to generalise to a wider sample of possible data observations from the same source. Moreover, the time-segments in a first-level GLM-Spectrum are likely to exhibit strong autocorrelation (see section 2.4) which would need to be accounted for before any permutation testing could provide a valid result (Friston et al., 2000; Woolrich et al., 2001).

## 2.10 Software implementation and dependencies

The analyses in this paper were carried out in Python 3.9 with core dependencies as numpy (Harris et al., 2020), scipy (Virtanen et al., 2020) and Matplotlib (Hunter, 2007). MNE python (Gramfort, 2013) was used for EEG/MEG data processing with OSL batch processing tools (Quinn et al., 2022). The spectrum analyses further depend on the Spectrum Analysis in Linear Systems toolbox (Quinn and Hymers, 2020) and glmtools[5]. All code used to run analyses and generate the figures in this paper are available online[6].

## 2.11 The LEMON Dataset

### 2.11.1 EEG Preprocessing

All data pre-processing was carried out using MNE-Python and OSL using the OSL batch pre-processing tools. Resting-state EEG recordings from 191 individuals of an open source dataset (Babayan et al., 2019) were analysed. The raw data for each subject is a resting-state EEG recording from a 62-channel (61 EEG and 1 EOG) cap using a BrainAmp MR plus amplifier. The channels were in the 10-10 layout and referenced to FCz. Sixteen minutes of data were recorded in one-minute blocks alternating between eyes closed and eyes open resting-state. Data were acquired with a bandpass filter between 0.015 Hz and 1 kHz at a sampling frequency of 2500 Hz. The remaining acquisition details are reported in (Babayan et al., 2019).

The raw data were first converted from Brainvision files on disk into MNE-Python Raw data objects. The continuous data were bandpass filtered between 0.25 Hz and 125 Hz using an order-5 Butterworth filter. A notch filter was then used to suppress line noise at 50, 100 and 150 Hz. Bad channels were automatically identified using the generalised-extreme studentized deviate (G-ESD;Rosner (1983)) routine to identify outliers in the distribution of variance per channel over time. The data were then resampled to 250 Hz to reduce space on-disk and ease subsequent computations. Independent Component Analysis (ICA) denoising was carried out using a 30 component FastICA decomposition (Hyvarinen, 1999) on the EEG channels. This decomposition explained an average of 99.2% of variance in the sensor data across datasets. Artefactual components containing blinks were automatically identified by correlation with the simultaneous V-EOG channel. ICA components linked to saccades were identified by correlation with a surrogate H-EOG channel, i.e., the difference

[5] `https://pypi.org/project/glmtools/`
[6] `https://github.com/OHBA-analysis/Quinn2022_GLMSpectrum`

between channels F7 and F8. Between 2 and 7 components were rejected in each dataset, with an average of 2.66 across all datasets. The two ICs that correlated strongest with the V-EOG and H-EOG channels were separately retained for later use in the GLM design matrix.

The continuous sensor data were then reconstructed without the influence of the artefactual V-EOG and H-EOG components. Bad segments were identified by segmenting the ICA-cleaned data into arbitrary 2-second chunks (distinct from the STFT time segments) and using the G-ESD algorithm to identify outlier (bad) samples with high variance across channels. An average of 31 seconds of data (minimum 6 seconds and maximum 114 seconds) were marked as bad in this step. This procedure is biased towards low-frequency artefacts due to the 1/f shape of electrophysiological recordings. Therefore, to identify bad segments with high-frequency content, the same procedure was repeated on the temporal derivative of the ICA-cleaned data. An average of 27 seconds of data (minimum 2 seconds, maximum 109 seconds) were marked as bad when using the differential of the data.

To retain consistent dimensionality across the group, any bad channels were interpolated using a spherical spline interpolation (Perrin et al., 1989) as implemented in MNE-Python. Finally, the spatial gradient between each channel and its distance from the reference sensor (FCz), is attenuated by computing the surface Laplacian (or current source density) of the sensor data. The surface Laplacian data is reference free and has sharper spatial topographies than the raw EEG; though this is complex computation that is dependent on several hyperparameters, and which may reduce sensitivity to deeper sources (Kayser and Tenke, 2015).

### 2.11.2 First-Level GLM-Spectrum

A 'first-level' analysis model the data within each individual participants EEG data. The STFT is computed from the preprocessed sensor time-series from each dataset using a 2 second segment length, a 1 second overlap between segments and a Hanning taper. The 2 second segment length at the sample rate of 250Hz gives a resolution of around 2 frequency bins per unit Hertz in the resulting spectrum. The short-time magnitude spectrum is computed from the complex valued STFT and the frequency bins ranging between 0.1Hz and 100Hz taken forward as the dependent variable in the first-level GLM-Spectrum for that dataset. The GLM design matrix is specified with eight regressors (Figure 1). A single constant regressor models the intercept of the data whilst two non-zero mean regressors model the eyes open and eyes closed effect. The fourth regressor is a z-transformed covariate describing a linear trend over time. Two non-zero mean confound regressors tracked the sum of the number of samples within each STFT time segment that were marked as bad samples (these are the bad samples assumed to be associated with lower frequency content) and differential bad samples (the bad samples associated with higher frequency content). Rather than a continuous regressor containing the number of bad segments, we could have used a categorical regressor with a value of one when there were any bad samples the STFT time segments, and zeros otherwise. We chose the continuous approach to allow the model to distinguish STFT time segments that contain a brief artefact, from STFT time segments that contain only artefactual samples. Finally, two further non-zero mean confound regressors are constructed from absolute value of the V-EOG and H-EOG independent component time-courses. Each covariate is subjected to the same windowing as the STFT before the values in each window are summed to create a vector of regressor values. The four confound regressor values are scaled between zero and one, and the linear trend is z-transformed.

A range of contrasts are specified to quantify critical hypothesis tests. The overall mean is modelled by a contrast summing the constant, eyes open and eyes closed

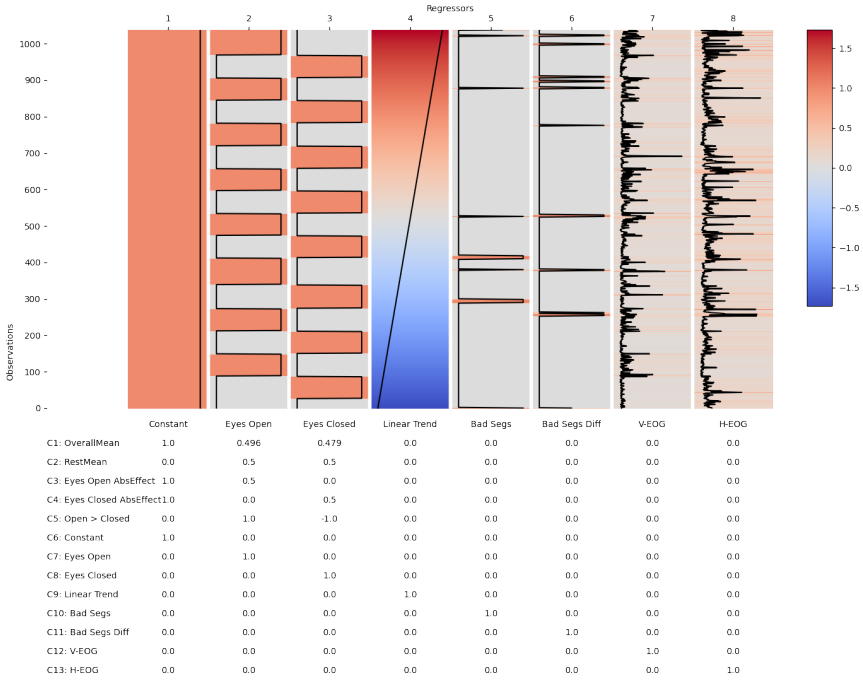


**Fig 1. An example first-level design matrix and contrast matrix for a single subject.** The matrix shows the design matrix with individual regressor in columns. The table shows the contrast matrix with corresponding weightings for each regressor. The efficiency of this design matrix is summarised in Supplemental section F.

regressors together weighted by the proportion of ones in each regressor (Contrast 1, Figure 1). A t-test between the spectrum in the eyes-open and eye-closed conditions is specified with a differential contrast (weighted [1, -1], in the direction of eyes open minus eyes closed; Contrast 5; Figure 1). Finally, separate one-sample tests are specified for each covariate with contrasts containing a single one for a given regressor (Contrasts 9 to 13; Figure 1). A design matrix and contrast table for a single dataset is shown in Figure 1. The model parameters were estimated using the Moore-Penrose peudo-inverse method and no statistical assessment was carried out at the first level.

### 2.11.3 Structural MRI Processing

Individual anatomical details were extracted from T-weighted structural MRI scans downloaded from the LEMON data server (Babayan et al., 2019). All images were processed using the FMRIB Software Library (Woolrich et al., 2009). Images were reoriented to standard Montreal Neurological Institute (MNI) space, cropped, and bias-field corrected. FMRIB's Linear Registration Tool (FLIRT; Greve and Fischl (2009); Jenkinson et al. (2002); Jenkinson and Smith (2001)) was used to register to standard space before brain extraction was performed using BET (Smith, 2002). Brain images were segmented into different tissue types (grey matter, white matter, CSF etc) using FMRIB's Automated Segmentation Tool (FAST; Zhang et al. (2001)). The voxel count for each tissue type was extracted and normalised by the individual's total brain volume (also computed by FAST) to create a percentage. The total brain volume and

individual percentage of grey matter were carried forward as group-level covariates in the GLM-Spectrum.

### 2.11.4 Group-Level GLM-Spectrum

We now carry out a "group-level" analysis to combine the first-level results and describe between subject variability with another GLM. As described in section 2.8, the cope-spectra of each first-level GLM was used as the dependent variable in the group-level GLM. The group-level design matrix contained categorical regressors coding the age group of each participant and covariates corresponding to variability in participant sex, head size and relative grey matter volume. A contrast was defined to estimates the mean across all participants and a second to estimate the difference between young and old participants. Finally, one-sample t-tests were specified for each covariate to test whether the regression coefficient significantly differed from zero.

The group-level design matrix was applied separately to several first-level contrasts. The overall mean, the difference between eyes-open and eyes-closed rest, and the main effect of each covariate. Statistical significance in the group-level t-spectra was assessed using cluster-based non-parametric permutations based on sign-flipping or row-shuffle permutations. The group model parameter estimates were computed using the Moore-Penrose pseudo inverse. A cluster forming threshold of t=3 was used for all permutations, except for a threshold of t=6 used for the group average of the first-level covariates, as very strong effects were observed in the artefact sources.

# 3 Results

## 3.1 First-level covariate spectra on a central EEG channel

Figure 2 summarises the first-level GLM-Spectrum analysis of a single channel (Pz) from an exemplar resting-state EEG recording. The pre-processed EEG time series (Figure 2A) was split into 2 second time segments with a 50% overlap (Figure 2B), modified by a Hann window (Figure 2C) and transformed into the frequency domain using a Short-Time Fourier Transform (STFT; Figure 2D). Each column of this STFT contains the time course of the magnitude at each frequency and constitutes the dependent variable in a first-level GLM. The first-level GLM (see methods section 2.11.2) models this variability over time in relation to the resting conditions, artefacts detected in the data and the electrooculogram (EOG). The final first-level design matrix had eight regressors (Figure 2E) modelling the two resting-state conditions, a linear trend over time and four potential dynamic confounds. The full design matrix and contrast specification for the entire run can be seen in Figure 1.

The first-level GLM was fitted separately for each frequency bin using a standard ordinary least squares routine. The average magnitude spectra for the eyes open and eyes closed rest periods are quantified by two cope-spectra (Figure 2F) specified by first level contrasts 3 and 4 (Figure 1). Both cope-spectra showed a 1/f-type structure and a prominent alpha peak around 9 Hz. The eyes open > eyes closed contrast (the regressor was coded to have ones for eyes open and minus ones for eyes closed; specified in contrast 5 in Figure 1) had negative values in the cope-spectrum indicating that spectral magnitude was larger in the eyes closed condition across a range of frequencies, peaking around the alpha range (Figure 2G – top left panel). The square of the standard error of the estimates is shown in the varcope-spectrum (Figure 2G – top right panel) and indicates where the estimate of the mean was least certain. This roughly followed the shape of the spectra in Figure 2F, showing a clear alpha peak and a weak 1/f trend. This is an example of a close relation between cope and varcope estimates that can lead to effects with large effects in the beta-spectrum being substantially less prominent in the t-spectrum. We used a varcope smoothing correction before computing pseudo-t-spectra to account for this effect (Nichols and Holmes, 2001) (see methods section 2.5 and supplemental section 7.5 for more details). The final pseudo t-spectrum contained a full spectrum of t-values for the contrast between the two resting conditions (Figure 2G – bottom panel). The large magnitude, negative t-values in alpha and surrounding frequencies qualitatively indicated a greater magnitude in the eyes closed condition. In sum, this shows a full spectrum perspective on the 'alpha reactivity' or 'alpha blocking' effect (Adrian and Matthews, 1934) the is most commonly assessed within a-priori frequency bands (Babiloni et al., 2011; Wan et al., 2018).

Next, we visualised the results from the dynamic confound regressor created from the marked bad segments estimated on the differential of the EEG data (Figure 2H). The cope-spectrum of this regressor was mostly positive apart from the alpha (9-12 Hz) range (Figure 2H – top left panel). The square of the standard error of the estimate shown by the varcope-spectrum was highest around the alpha peak frequency. This pattern was very similar to other varcope-spectrum of the condition contrast (figure 3H – top right panel). The largest values in the pseudo-t spectrum are in relatively high frequencies (25 to 100 Hz). This qualitatively indicates, as expected, that the differential bad segments are particularly sensitive to high-frequency noise.

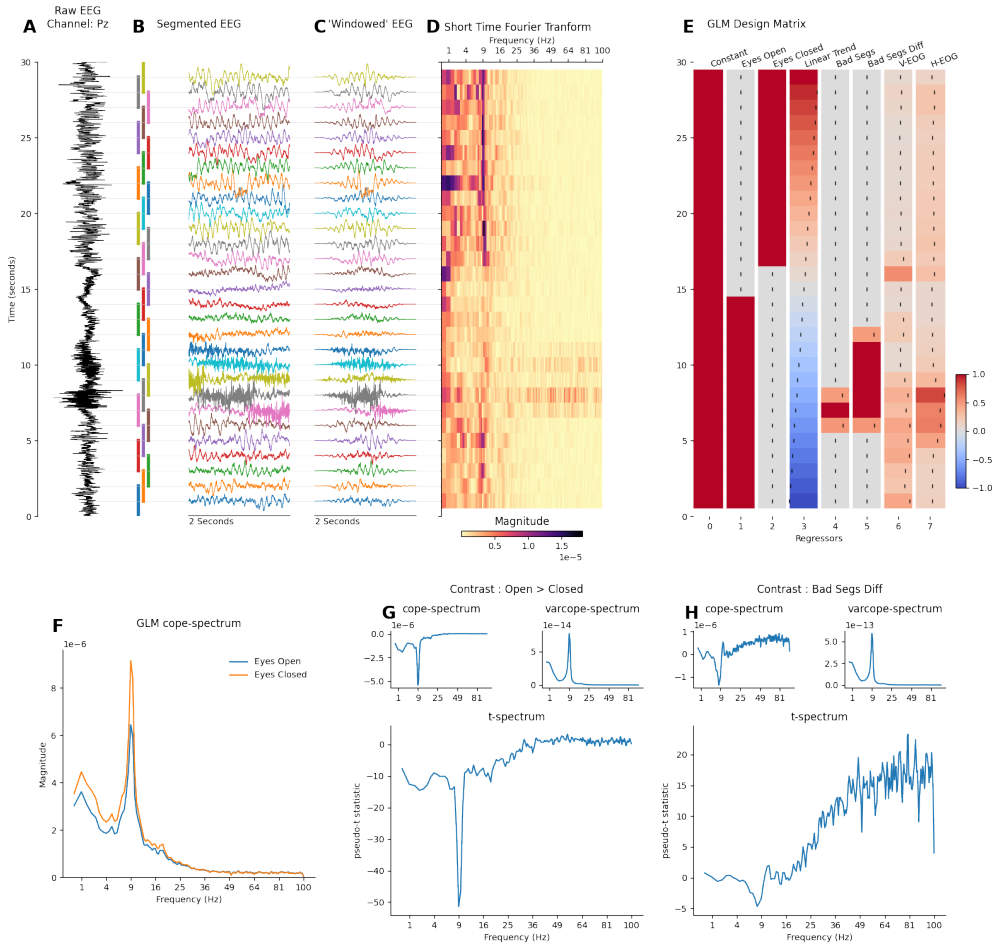


**Fig 2. First-level (i.e. within-session) GLM-Spectrum description during alternating eyes open and eyes closed resting-state from channel Pz in a single EEG recording.**

**A:** A 30-second segment of pre-processed EEG time-course from sensor Pz.
**B:** EEG time-course segmented into 2-second sliding windows with 50% overlap.
**C:** Windowed data segments modified by a tapered Hann window function.
**D:** Short time-Fourier transform computed with the FFT of each windowed data segment. Each column of this matrix (change in magnitude of a single frequency over time) is the dependent variable to be described by the GLM.
**E:** The GLM design matrix containing condition, covariate and confound regressors.
**F:** The GLM beta-spectra for the two regressors modelling the spectrum during eyes-open and eyes-closed rest (contrasts 3 and 4 in Figure 1).
**G:** The cope-, varcope- and pseudo t-spectrum for a differential contrast between the eyes open and eyes closed conditions as specified in contrast 5 in Figure 1.
**H:** The cope-, varcope- and t-spectrum for a mean contrast on the differential bad segments confound regressor as specified in contrast 11 in Figure 1.

## 3.2 First-level spectral analysis on whole head EEG

So far GLM-Spectrum method has been applied to univariate data (i.e., single-channel EEG data), but it can be readily extended to a full multi-channel dataset. To model the GLM-Spectrum across channels, a separate GLM using the same design matrix was fitted to each channel and frequency bin. This provides a description of spectral effects over frequency and space. Accordingly, we extended the resting-state model to the 61-channel whole head EEG recording. The design matrix and contrast specification were the same as the single-channel analysis.

The beta-spectrum computed from the condition regressors showed the familiar 1/f slope and prominent occipital alpha features in both resting-state conditions. The GLM analysis was identical to the single channel results (Figure 2) but now can include spatial distributions alongside the frequency spectrum. Qualitatively, the eyes-open condition (Figure 3A) had a smaller alpha peak than the eyes-closed condition (Figure 3B). Both conditions had a similar topography in this subject. The pseudo t-spectrum of the contrast between eyes open and eyes closed rest showed a large, negative effect peaking around the alpha range (Figure 3C) as seen in the single channel example (Figure 2G). This difference had a spatial maximum in posterior-central regions, replicating the occipital-parietal location of the alpha reactivity effect widely reported in the literature (Babiloni et al., 2011; Wan et al., 2018).

We can qualitatively evaluate the t-spectra of these first level results, though in this work, a full statistical analysis is reserved for the group level (see methods section 2.4 and 2.9 for details), The group-level best reflects the analyses typically carried out in cognitive or clinical neuroscience research studies. The t-spectra quantify the statistical association between each regressor and the time-varying spectrum. This effect is then visualised with a model-projected spectrum averaged across channels for each contrast. The linear trend showed substantial pseudo t-values around the alpha range, though its model projected spectra suggest that this is a subtle effect (Figure 3D). The bad segments (Figure 3E) and bad segments estimated on the differential of the preprocessed time-series (Figure 3F) show similar patterns peaking at relatively low (<4Hz) and high (>25Hz) frequency ranges. The pseudo t-spectrum showed substantially higher values for bad-segments detected on the differential suggesting that these artefacts were more strongly associated with dynamics in the spectral magnitude over time-segments. The size of this effect is visualised more intuitively in the model projected spectrum (Figure 3F – bottom panel) which shows the substantial increase in both low and high frequency magnitude in time segments with large amounts differential bad segments. Finally, the V-EOG (Figure 3G) and H-EOG (Figure 3H) covariates both showed large t-values in relatively low frequencies (around 1Hz). The V-EOG had a large negative effect around the alpha range, suggesting that time segments with high V-EOG activity were associated with lower alpha magnitude. In contrast, the H-EOG showed an additional positive effect in high frequencies suggesting that segments with high H-EOG activity are associated with higher high frequency spectral magnitude. In particular, the complex pattern of effects in the V-EOG t-spectrum manifests as segments with high V-EOG activity showing a decrease in alpha magnitude and an increase in alpha frequency.

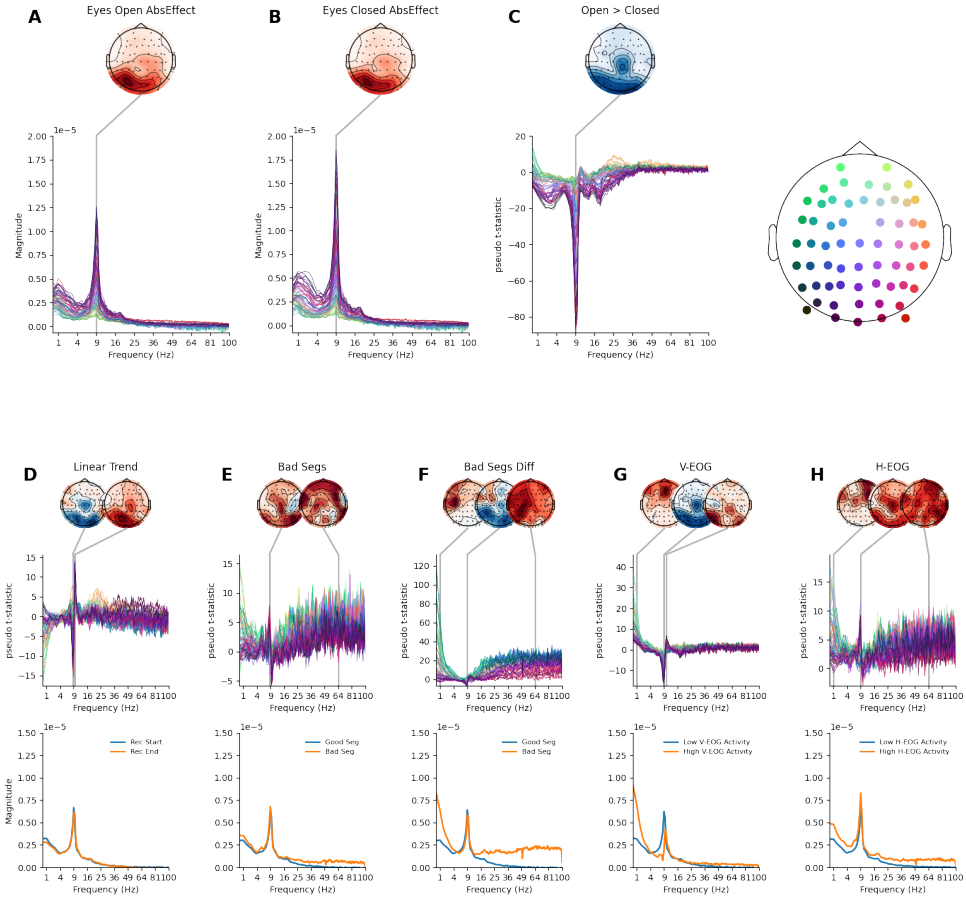


**Fig 3. GLM-Spectrum fits for alternating eyes-open and eyes-closed resting-state EEG for a single participant.** Mean magnitude spectrum estimates for each channel and frequency bin. The topography (top right) provides location-colour coding used in the pseudo t-spectra throughout the figure. The colour range of each topography is set range between plus and minus the maximum absolute value of the data plotted. The contrasts shown in this figure are detailed in supplemental section H.

**A:** Beta-spectrum for the eyes open condition regressor. The topography shows the spatial distribution of spectral magnitude at 9 Hz

**B:** Beta-spectrum for the eyes closed condition regressor, layout is same as in A.

**C:** Pseudo t-spectrum for the contrast between the eyes open and eyes closed conditions.

**D:** Pseudo t-spectrum spectrum for the linear trend covariate (top). Model-predicted magnitude spectra averaged across all sensors for the extrema of the predictor, which in the case of a linear trend regressor corresponds to the start and end of the scan (bottom).

**E:** Pseudo t-spectrum spectrum for the bad segment confound (layout same as for D), model-projected spectra are shown for good and bad segments.

**F:** Pseudo t-spectrum spectrum for the differential bad segment confound (layout same as for D), model-projected spectra are shown for good and bad segments.

**G:** Pseudo t-spectrum spectrum for V-EOG confound (layout same as for D), model-projected spectra are shown for zero, and the maximum observed, V-EOG activity.

**H:** Pseudo t-spectrum spectrum for H-EOG segment confound (layout same as for D), model-projected spectra are shown for zero, and the maximum observed, H-EOG activity.

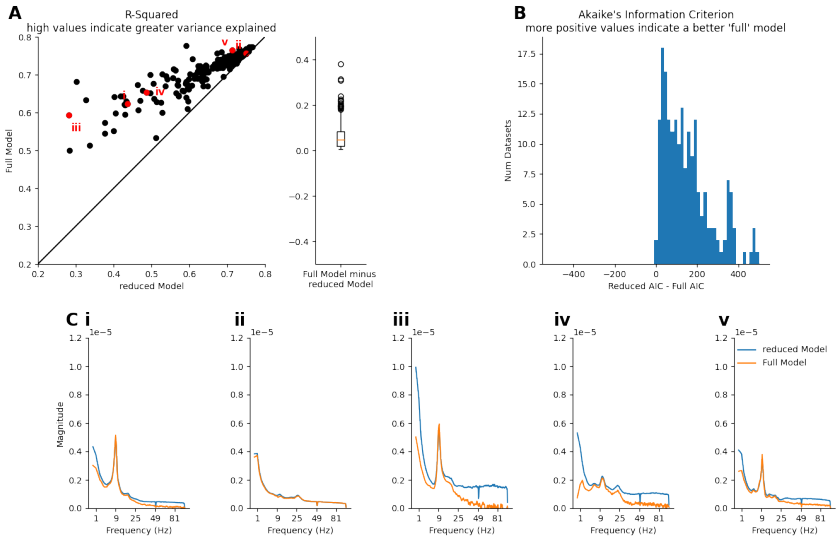


**Fig 4. Effect of first-level confound variables on mean spectrum estimates.**
**A:** The coefficient of variation of the full model and the reduced model (condition terms only) for all datasets. Points lying to the left of the x=y boundary are datasets where the full model explained more variance than the reduced model. The red dots are datasets visualised in c. The box plot shows the difference between the full and reduced models and indicates that the variance explained was improved in the full model for all datasets.
**B:** The distribution of differences between AIC estimates for the full and reduced models across all 191 datasets. All datasets lie on the positive side of the x-axis indicating that the inclusion of additional covariates and confounds improved the model in all cases.
**C:** Closer visualisation of the average beta-spectra across all channels from five example datasets (highlighted in red in 6A). Ci is the dataset used in the figures 2 to 5.

## 3.3 Model assessment across datasets

Next, we build on the single subject exemplar result by exploring the effect of the covariate and confound regressors across 191 EEG recordings from the LEMON dataset. Each dataset was modelled individually using the same pre-processing, design specification and model fit as the single subject example above. The overall mean variance explained was computed and averaged across frequencies and channels for both a full model and a reduced model. The reduced model only contains the constant and two condition terms (i.e., eyes open and eyes closed), excluding other covariates and confounds. It acts as a benchmark analysis enabling us to explore how the addition of covariate and confound variables affects spectrum estimates.

The R-squared values for the full and reduced models are compared in Figure 4A. All datasets in this study lie to the left of the x=y boundary, indicating that the full model explained more variance than the reduced model in all datasets. The R-squared metric is limited in that a more complex model can always be expected to explain more variance than a simpler one. We use it here only as an interpretable description of how much improvement is seen in each individual dataset. The overall distribution of full model minus reduced model r-squared values show that the median improvement was around 5%, ranging from <1% up to 45% in one exceptional case. Akaike's Information Criterion (AIC; Akaike (1974)) provides a more principled comparison that accounts for model complexity. This difference between AIC estimates for the full and reduced model for each dataset indicates that the inclusion of additional covariate and

confound regressors improved the model in all datasets, justifying the additional complexity (Figure 4B). More formal model comparisons could be carried out by a cross-validation analysis.

Here, we have focused on model assessment metrics that can be computed from the residuals of the GLM fit. The R-squared metric and AIC as used above use the residuals to assess goodness of fit to help select between models. Many further assessments and diagnostics could be performed on the GLM-Spectrum. One example would be diagnostics that explore in detail whether the model assumptions have been violated (see methods section 2.4 and supplemental section 7.3 for an example using the Durbin-Watson statistic). Future work could extend this assessment to include cross-validation methods from machine learning including exploration of out of sample prediction errors (Stone, 1974).

The differences between datasets can be driven by several factors including variability in neuronal oscillations, acquisition noise, and physiological noise. The overall mean cope-spectrum (averaged across all channels) for the full and reduced models are shown for five example datasets in Figure 4C). The first dataset is the example used in previous analyses, a modest attenuation of low- and high-frequency magnitude can be seen when including confound regressors. In contrast, very little change can be seen for datasets ii and v. Finally, the confound regressors have a substantial impact on the overall mean spectrum of datasets iii and iv. In particular, the confound regressors remove a large amount of variability in low and high frequencies in dataset iv. Critically, this shows that the GLM-Spectrum can adaptively treat noise across datasets. No denoising is applied when the regressor cannot explain variance in the time-varying spectrum but the impact of denoising can be substantial when specific patterns of structured noise are associated with the confound regressors.

Next, the variance explained by each regressor within each frequency bin was summarised across all 191 participants. The R-squared value was computed as a percentage for the full model and for a simplified model containing only one of the regressors in turn (Figure 5A). This provides an upper estimate of the amount of variance each individual regressor might explain. The full model explained between 50% and 80% of the temporal variability in the magnitude spectrum across all channels and frequencies ('Full Model', Figure 5A). The average variance explained across the whole group was relatively constant across frequency, though variability was high across individual datasets, particularly in higher frequency ranges. The simplest reduced model only contained only a constant regressor ('Constant Only'; Figure 5A); this model is directly equivalent to a standard time-averaged magnitude periodogram. It showed a broadly similar pattern to the full model, though the variability across individual datasets was larger. The eyes-open and eyes-closed regressors explained between 20% and 50% of variability on their own ('Eyes Open Only' and 'Eyes Closed Only'; Figure 5A). The eyes closed regressor shows a peak in the alpha range, reaching around 60% in some participants. In contrast, the eyes open regressor tended to explain less variance overall and was more variable across participants in higher frequencies.

The linear trend regressor explained the least variance overall, the average across datasets only peaking around 2-5% ('Linear Trend Only'; Figure 5A). The linear trend explained up to around 20% of variance in high frequencies for a small number of participants, though this was not consistent overall. The average across datasets for the bad sement confound regressors ranged between 5% and 20%, though this value was highly variable across individual datasets ('Bad Segs Only', 'Bad Segs Diff Only'; Figure 5A). Finally the V-EOG and H-EOG confound regressors explained an average of 40% and 50% of variance respectively there was substantial variability between datasets ('V-EOG Only', 'H-EOG Only'; Figure 5A). Both EOG regressors were highly

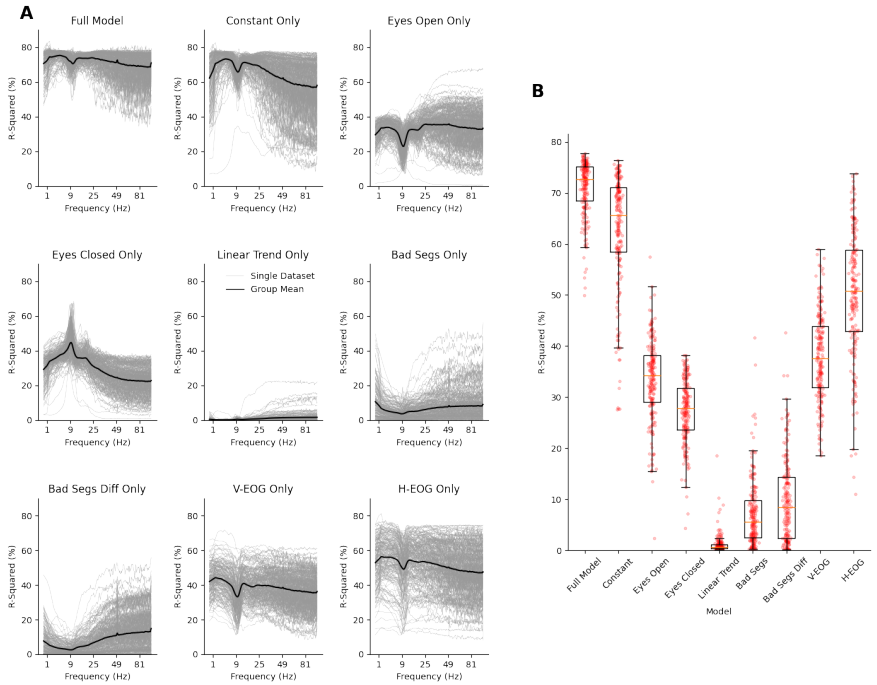


**Fig 5. The distribution of variance explained by the model across frequency and participants.**

**A:** The frequency spectrum of R-squared value averaged across channels for each dataset (grey lines) and the average across all datasets (black lines). Each subpanel shows the variance explained for a single GLM-Spectrum model. **B:** The distribution of R-Squared values averaged across frequency and channels for each dataset for each GLM-Spectrum model. Each red dot represents a dataset with the box plot representing their distribution.

variable between datasets, ranging between 20% and 80% of variance explained.

The model fit performance has variability both within individual first-level models and between subjects. As such, the variability in R-squared we observe here reflects a combination of these two sources. We can visualise the between-subject variability (neglecting the variance within each dataset) by taking the average R-squared across all channels and frequencies as represented by the distributions in Figure 5. This illustrates the adaptive nature of the confound regression. These confound regressors explain very little difference in clean datasets with relatively few artefacts but can absorb substantial variability in noisier recordings. This individual variability is summarised in Figure 5B, each red dot represents the average R-Squared across frequencies and channels for each dataset for each model. The variance explained by the bad segment confound-regressors is close to zero for many participants, though the upper end of these distributions reaches 30%-40% of all variance explained in some datasets. The EOG confounds have a range of 15% to 75% of variance explained in each dataset, they tend to explain more variability than the bad segments, but remain widely varying across recordings.

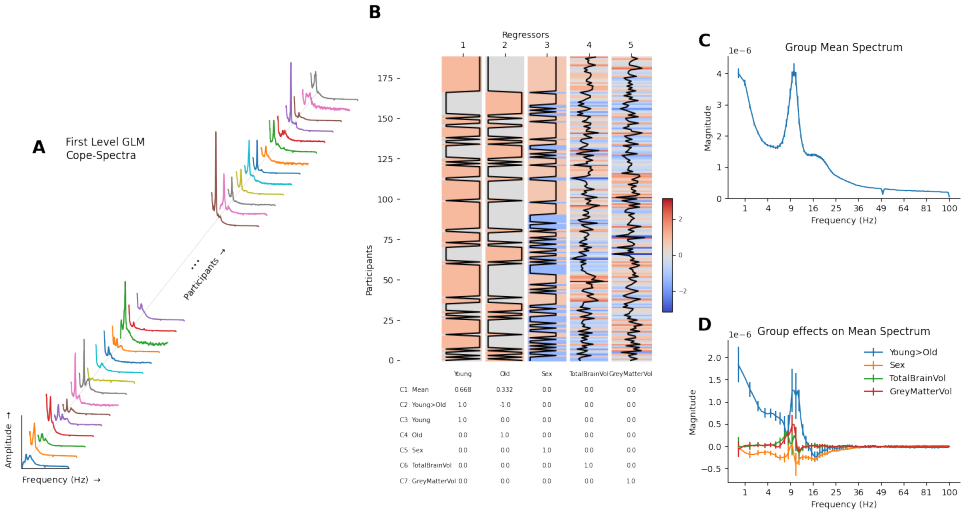


**Fig 6. Group-level GLM-Spectrum describing a group mean and variability associated with two between-subject factors.**
**A:** The data modelled by the group-level GLM are the first-level GLM-Spectra across all participants. A GLM is fit separately for each channel, frequency bin and first-level contrast. **B:** The group-level design matrix. The first and second regressors are categorical predictors coding female and male participants. **C:** The group-level estimate obtained from the first contrast coding for the average of the two regressors (contrast 1). Error bars indicate the varcope of the group contrast. **D:** The group-level effects for the difference between female and male participants (contrast 2, weighted [1, -1]) and the three covariate contrasts (contrasts 5, 6 and 7), quantifying the effect of sex, total brain volume and normalised grey matter volume respectively. Error bars indicate the varcope of the group contrast.

## 3.4 Group-level design matrix and contrasts

The GLM-Spectrum framework can be extended to group analyses by carrying a set of first-level results to a second-level GLM (See methods section 2.8). This group-level analysis models between-subject variability across independent first-level GLM-Spectra. These multilevel, hierarchical models are well established in neuroimaging (Beckmann et al., 2003; Friston et al., 2002; Friston, 2007; Woolrich et al., 2004), and the existing theory applies to the GLM-Spectrum.

The group-level GLM was fitted to the first-level cope-spectra (Figure 6A) across all datasets separately for each channel, frequency bin and first-level contrast (see methods section 2.11.4). The group-level design matrix contained two condition regressors modelling the mean across subjects for younger and older participants separately and three z-transformed parametric covariates modelling between-subject variability in sex, total brain volume and relative grey matter volume (Figure 6B). Two group contrasts were defined alongside the main effects. One overall average that modelled the sum of the young and old groups (Contrast 1; Figure 6B) weighted by the the number of participants in each group. A second contrast quantified the linear group difference (Contrast 2; Figure 6B). Finally, a set of main effect contrasts were also defined for each regressor (Contrasts 3 to 7; Figure 6B). The final fitted model contains a group-level beta-spectrum that describes the linear effect of a group regressor across separate datasets. The group-level GLM returns beta-spectra for the overall mean spectrum (Figure 6C) as well as contrasts and main effects (Figure 6D). At the

group-level, the error bars now indicate the standard error of the fitted mean across participants (rather than across STFT time windows, as in the first-level).

## 3.5 Group effects of age and eyes open versus eyes closed

Next, we explored how the GLM-Spectrum varies across resting conditions and participant age. Therefore, two main-effect contrasts and their interaction were explored. Two-tailed, non-parametric, cluster (with clusters formed over frequencies and sensors) permutation tests were used to establish statistical significance for all group level analyses.

We first computed the group average of the within-subject difference between eyes-open > eyes-closed rest. Specifically, we computed the *Mean* group-level contrast (Contrast 1; Figure 6B) on the *eyes open > eyes closed* first-level contrast (Contrast 5; Figure 1). Non-parametric cluster permutation testing indicated two significant clusters (Figure 8A). The first cluster showed a negative effect (indicating greater magnitude in the eyes-closed condition) in the lower frequency range (<20 Hz) across almost all channels, though the effect peaked around the alpha range in occipital channels. This posterior cluster matched the expected occipito-parietal source of the reactivity effect (Wan et al., 2018). The second cluster showed a positive effect (indicating higher magnitude in the eyes open condition) in the higher frequency range (20-50 Hz) across all channels with the largest effect in bilateral frontal regions. This cluster potentially reflects residual eye movements that have not been accounted for by ICA or the first-level artefact regression.

Further, we computed the difference in the time-averaged first-level spectra between the younger and older adults. This corresponds to computing the *Young > Old* group-level contrast (Contrast 2; Figure 6B) on the *Overall Mean* first-level contrast's cope-spectrum (Contrast 1; Figure 1). The group-level pseudo t-spectrum for this showed three significant clusters. The first cluster covered low frequencies (<8 Hz) and much of the electrode array peaking in frontal and occipital channels (Figure 8B). The positive t-values within this cluster indicated that spectral magnitude was higher for younger participants, consistent with previously reported decreases in delta and theta power in older adults (Klimesch, 1999).

The second and third clusters are similar and likely split in frequency by the notch filter for line noise. These clusters cover a wide frequency range (14-48 Hz and 52-100 Hz) and cover many sensors, peaking in bilateral central sensors around the beta frequency range (Figure 8B). The t-stats in these clusters were negative, indicating that older participants had higher magnitude in this frequency range. This replicates literature showing higher beta power in older adults (Xifra-Porxas et al., 2019). In addition, the change in overall spectral shape qualitatively supports indications that older adults have a flatter 1/f slope in the EEG spectrum (Merkin et al., 2022; Voytek et al., 2015), though we did not explicitly quantify 1/f slope here.

No significant cluster for an age difference was identified in the alpha range, though individual pseudo t-statistics reach around 5. This null effect may relate to the choice of sensor normalisation during pre-processing (Klimesch, 1999). In addition, the choice of a 0.5 to 100 Hz frequency range may be too wide to assess any relatively narrow band alpha changes in the presence of large broadband effects in higher frequencies.

Finally, we explored whether the within-subject difference in eyes-open and eyes-closed resting-state changed between the younger and older adults. Specifically, this corresponds to the *Young > Old* group-level contrast (Contrast 2; Figure 6B) computed on the *eyes open > eyes closed* first-level contrast (Contrast 5; Figure 1). Non-parametric permutation testing identified two significant clusters (split by the notch filter for line noise). The clusters spread from high alpha up throughout the

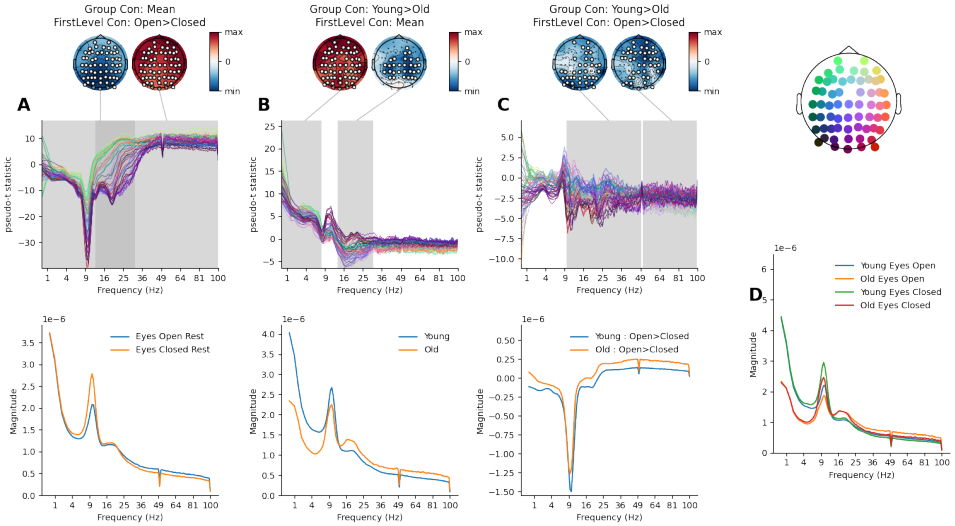


**Fig 7. Higher order GLM-Spectrum group-level results.**. The topography (top right) provides location-colour coding used in the pseudo t-spectra throughout the figure. In all cases, statistical significance is assessed by sensors x frequency cluster permutation testing and is indicated in grey. The colour range of each topography is set range between plus and minus the maximum absolute value of the data plotted.
**A:** The within-subject contrast between eyes-open and eyes-closed conditions, averaged across all participants. Model-predicted magnitude spectra averaged across all sensors for the extrema of the predictor (bottom).
**B:** The between-subject difference in average magnitude between young and old participants. Layout is the same as for A.
**C:** The interaction effect exploring whether the eyes-open>eyes-closed contrast varies between young and old participants. Layout is the same as for A.
**D:** The averaged GLM-Spectra for the two conditions and two groups.

spectrum and a range of sensors (Figure 8C). This effect indicates areas where older adults show a larger increase in spectral magnitude when transitioning from eyes closed to eyes open during resting state. Interestingly, there is no indication of an interaction effect in the low to mid alpha range. The interaction can be qualitatively summarised by plotting the beta-spectrum separately for each of the underlying four mean levels (Figure 8D).

## 3.6 Group average of first-level cope-spectra.

Group analyses can be used to quantify between-subject effects in the cope-spectra of the first-level covariate regressors. This creates a statistical map identifying the effect of each potential artefact source across channels and frequencies. Statistical significance is established using two-tailed cluster-based permutation testing using a higher cluster forming threshold of t=6 (with clusters formed over frequencies and sensors), due to the very large effects observed here.

We first visualised the group spectra (averaged across younger and older participants) separately for the two resting-state conditions. Specifically, this corresponds to the *Mean* group-level contrast (Contrast 1; Figure 6B) computed on the *eyes open* and the *eyes closed* first-level contrasts separately (Contrasts 3 and 4; Figure 1). The expected 1/f and alpha peak structure was visible during eyes-open

(Figure 8A) and eyes-closed (Figure 8B) resting state, with a qualitatively larger alpha peak during eyes closed. The alpha peak in both conditions had a clear posterior-dominant topography.

The first-level linear trend regressor is expected to be sensitive to slow drifts throughout the duration of the whole recording. The pseudo t-spectrum of the *Mean* group-level contrast (Contrast 1; Figure 6B) computed on the *Linear Trend* first-level contrast (Contrast 9; Figure 1) showed two significant clusters (Figure 8C). The first cluster showed a positive effect across all channels below 1 Hz, indicating that spectral magnitude in this cluster increases over the course of the recording. The second cluster indicated a positive effect in fronto-central sensors in the beta frequency range (15-25 Hz), again suggesting that spectral magnitude in this cluster increases over time.

The group average pseudo t-spectrum for the bad segment and differential bad segment regressors highlight the spectral profile of these artefacts. The *Mean* group-level contrast (Contrast 1; Figure 6B) computed on the *Bad Segs* first-level contrast (Contrast 10;  1) showed a strong positive effect at low frequencies (<2 Hz) across all channels (Figure 8D). In contrast, the *Mean* group-level contrast computed on the *Bad Segs Diff* first-level contrast (Contrast 11; Figure 1) showed three significant clusters. The first was a low-frequency effect (<2 Hz) across all channels (Figure 8E), similar to the bad segments regressor but a qualitatively weaker effect. In addition, the other two clusters show a broadband high-frequency effect across the whole head split by the notch filter for line noise (Figure 8E). These differences show that standard bad-segment rejection is strongly biased towards low-frequency artefacts and that identifying artefacts on the differential of the EEG signal can strongly increase sensitivity to high-frequency artefacts.

Finally, we computed the *Mean* group-level contrast (Contrast 1; Figure 6B) computed on the *V-EOG* and *H-EOG* first-level contrasts separately (Contrast 12 and 13; Figure 1). Cluster-based non-parametric permutation testing of the V-EOG artefact identified two significant clusters (Figure 8F). The first effect is an increase in low-frequency (<5 Hz) magnitude across a wide topography whilst the second cluster showed a decrease in alpha (around 7-10 Hz) magnitude peaking in occipital channels. The alpha range effect likely reflects real neuronal dynamics associated with eye blinks given that the activity is posterior and far away from the eye muscles and is therefore unlikely to have arisen from volume conduction. The H-EOG component (Figure 8G) shows two clusters across a broad spatial and spectral range, split by the line noise notch filter. In contrast to the relatively specific low-frequency and alpha effects in the V-EOG, artefacts associated with H-EOG are spectrally much broader also affecting the high end of the spectrum.

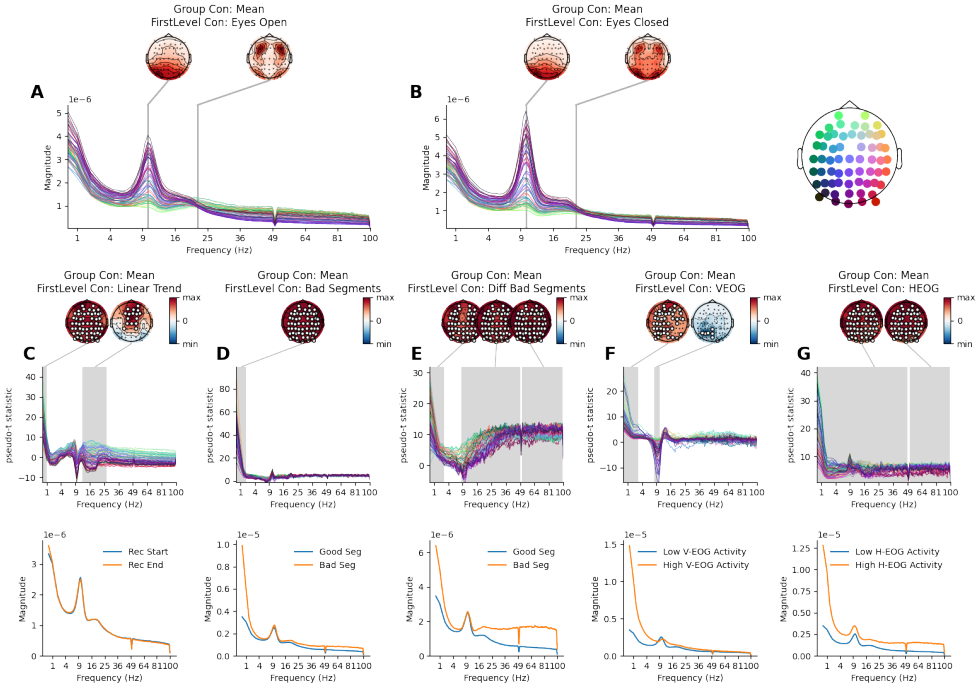


**Fig 8. Group-level group-averaged GLM-Spectrum results for each first-level regressor.** The topography (top right) provides location-colour coding used in the pseudo t-spectra throughout the figure. In all cases, statistical significance is assessed by sensors x frequency cluster permutation testing and is indicated in grey. The colour range of each topography is set range between plus and minus the maximum absolute value of the data plotted.

**A:** The group average of the first-level contrast that corresponds to the eyes-open cope-spectrum for all participants with topographies at 10 and 22 Hz. The spectrum is shown separately for each channel, whereby colour denotes channel location.

**A:** Same as A, but for eyes-closed resting-state.

**C-G:** For each of the first-level contrasts that correspond to the covariate and confound regressors: the group average GLM t-spectrum (top) and model-predicted magnitude spectra averaged across all sensors for the extrema of the regressors (bottom).

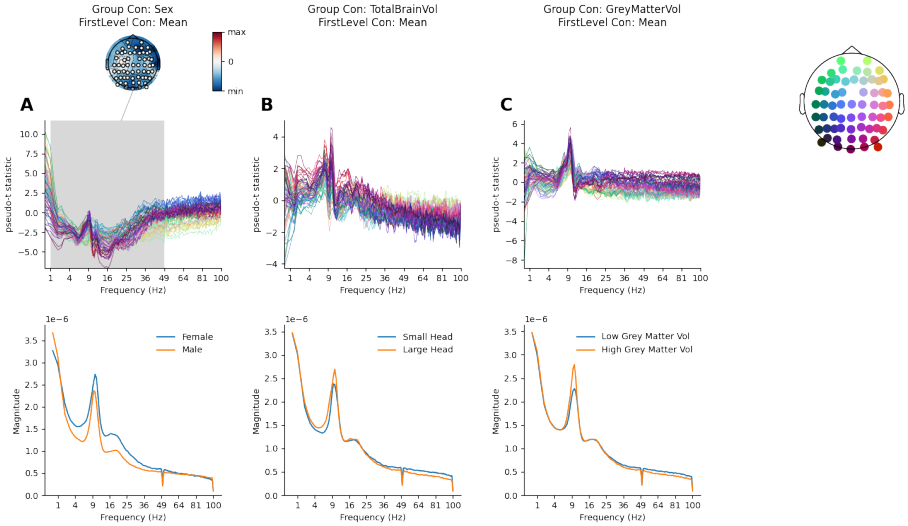


**Fig 9. Between-subject group covariate effects on the overall first-level mean.** The topography (top right) provides location-colour coding used in the pseudo t-spectra throughout the figure. In all cases, statistical significance is assessed by sensors x frequency cluster permutation testing and is indicated in grey. The colour range of each topography is set range between plus and minus the maximum absolute value of the data plotted.
**A:** The between-subject difference effect of sex on the average magnitude between females and males. The model projected spectra visualise the group differences (bottom).
**B:** Same as A for total brain volume. The model projected spectra visualise the spectrum at the smallest and largest head size.
**C:** Same as A for normalised grey matter volume. The model projected spectra visualise the spectrum at the smallest and largest grey matter volume.

## 3.7 Group-level covariate effects

The results so far have combined and contrasted group-level averages of the first-level results. We can also explore parametric variability between subjects, illustrating the potential of additional covariate and confound regression applied at the group level. Two-tailed non-parametric permutation testing was used to identify significant clusters with a cluster formed over frequencies and sensors with a threshold of t=3.

One possible group-level confound for the age contrast is that the LEMON dataset contains a different number of male and female participants. The small correlation between participant sex and age group indicates that these factors are not balanced. A separate group regressor indicating the reported sex of each participant was included to model between-subject variability relating to this factor, effectively partialling it out from the main age effect of interest in each group contrast. We visualise the overall effect of participant-reported sex on the first-level cope-spectra (averaged across eyes open and eyes closed resting-state); this corresponds to the *Sex* group-level contrast (Contrast 5; Figure 6B) computed on the *Overall Mean* first-level contrast (Contrast 1; Figure 1). A single significant cluster identified stronger spectral magnitude in female participants between 1 and 48 Hz, peaking around the alpha and beta frequency ranges (Figure 9A). Increased power in females relative to males has been previously reported in the EEG literature (Aurlien et al., 2004; Zibrandtsen and Kjaer, 2021). Further work is required to distinguish whether this is a true neuronal difference or

reflects simpler anatomical differences such as skull thickness.

Between subject variability associated with two anatomical covariates were modelled at the group level. The total brain volume of each participant and the proportion of grey matter relative to total brain volume. As before, the inclusion of these regressors ensures that the reported group effects are not biased by these anatomical factors. We separately computed the *TotalBrainVol* and *GrayMatterVol* group-level contrasts (Contrasts 6 and 7; Figure 6B) on the *Overall Mean* first-level contrast (Contrast 1; Figure 1). Non-parametric permutation testing did not identify any significant effects for either overall brain volume or relative grey matter volume (Figure 9B and C). Though these are null effects, the inclusion of these regressors in the group model enables a more refined interpretation of the other results. The inclusion of these confounds means that any variance they can explain can not be attributed to one of the other regressors. Specifically, this increases our confidence that the differences between younger and older adults is not caused by correlated variability in head size or relative grey matter volume.

Finally, we can visualise the distribution of variance explained in the first-level average spectra by the group GLM (Figure 10). As with the first level model assessment results (Figure 5), this gives us an intuition about which channels and frequencies are well described by each regressor in the group level GLM-Spectrum. The full group model is able to explain 60-90% of variability across participants (Figure 10A) with a spectral profile similar to the full model on the first level ('Full Model'; Figure 5A). The 'Young Only' and 'Old Only' reduced models explain substantially less variance (Figure 10B and C). More variance is described by the 'Young Only' regressor, though this overall shift likely reflects the larger number of young participants in the group analysis. The profile of R-squared values across frequency also differ between the young and old regressors, with the 'Young Only' regressor explaining more variance at lower frequencies and 'Old Only' explaining more variance at higher frequencies.

The three group covariates explain relatively low amounts of the overall between-subject variability. The 'Sex Only' model explains up to 4% of variance in posterior channels between 10Hz and 25Hz, and up to 5% of variance above 25Hz in frontal channels (Figure 10D). The 'Total Brain Volume Only' model shows a similar profile but explaining less variability overall, peaking at around 2% (Figure 10E). Finally, the grey matter volume covariate describes around 1% of variability in the high alpha range in posterior sensors, and up to 3% in high frequencies in frontal sensors (Figure 10F)

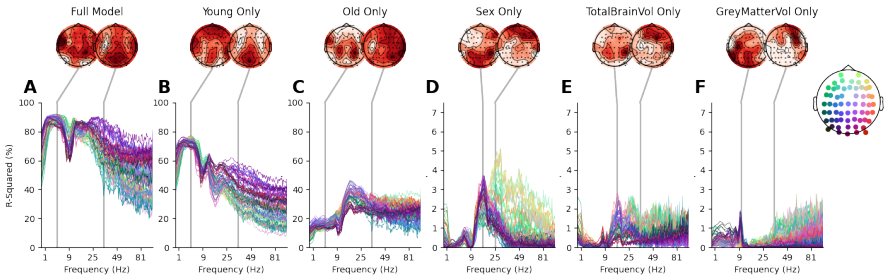


**Fig 10. The r-squared spectra for the full model and simplified models containing only a single regressor at a time.** The topography (top right) provides location-colour coding used in the pseudo t-spectra throughout the figure. The colour range of each topography is set range between zero and the maximum value of the data plotted. **A-F:** The r-squared spectrum for the full model explored in figure 4. The r-squared spectrum is shown separately for each channel, whereby colour denotes channel location.

# 4 Discussion

We have outlined the GLM-Spectrum framework and provided a tutorial overview of its function alongside a practical application. We have established the theory behind the GLM-Spectrum and provided practical guidelines for its use in data analysis. A first-level analysis was performed in which an alpha-reactivity effect was quantified alongside explicit modelling of a set of potential noise sources. The GLM beta-spectra for the noise sources showed substantial effects on the spectrum across the whole range of channels and frequencies. Critically, these are both quantified and partialled out of the main average by our multiple regression approach. Of particular interest is the alpha peak in the beta-spectrum of the V-EOG regressor. This is likely a true neuronal effect linked to blinking that cannot be removed by ICA but can be explicitly modelled by the GLM-Spectrum. Finally, we extended our analysis to the group level and explored the spectral differences between older and younger adults. Older adults were shown to have lower theta range (3-7 Hz) magnitude and higher magnitude in the beta and gamma ranges (>15 Hz). A range of within- and between-subject effects were explored and, crucially, we showed that the reported age effect is robust to differences in participant sex, head size or relative grey matter volume.

## 4.1 A comprehensive framework for spectrum analysis

The GLM-Spectrum is a practical combination of two well-established methodologies that modernises the statistics underlying the time-averaged periodogram, a long-standing and standard spectral estimation method (Bartlett, 1948, 1950; Welch, 1967). Specifically, we utilise multi-level general linear modelling (Friston, 2007; Woolrich et al., 2004), non-parametric permutation testing (Nichols and Holmes, 2001; Winkler et al., 2014), contrast coding and confound regression to extend the scope of classical time-averaged spectrum estimators.

We illustrate the GLM-Spectrum in an open EEG dataset by simultaneously quantifying and contrasting the spectrum of two alternating resting-state conditions whilst regressing out the effect of bad segments and eye movements. Both artefact types were associated with a strong group effect but diverse effects at the first level; the

denoising applied by the GLM was specific to each dataset and no denoising is performed in datasets where the spectrum showed no association with the noise covariates. Spectral differences between younger and older participants were quantified as a group-level contrast accounting for the effects of sex, brain volume and relative grey matter volume.

This approach is generalisable to a huge range of analyses. In principle, the GLM-Spectrum could be used in place of Welch's periodogram or other time-averaged spectrum estimate in any analysis pipeline. A very simple GLM-Spectrum analysis could be configured to be exactly equivalent to these standard approaches. In the simplest case, without first-level covariates the GLM-Spectrum provides a formal framework for multivariate whole-head group analysis of power spectra. Moreover, GLM-Spectrum allows for linear denoising of spectrum estimates wherever simultaneous recordings of potential artefact sources are available. In addition, covariate effects and contrasts can be readily defined to quickly compute spectra associated with specific external dynamics. For example, an early application of this method has used a GLM-Spectrum to compute power spectra associated with dynamic whole-brain functional networks in MEG (Gohil et al., 2022).

## 4.2 Covariate and confound regression for spectrum analysis

The GLM-Spectrum can characterise spectral changes associated with covariates and potential artefact sources. Standard ICA denoising removes artefacts that share the time-course of the artefact channel, In contrast, confound regression is exploratory across the spectrum. Denoising can be applied to any frequency band with dynamics associated with the segmented artefact time-course irrespective of the artefacts original spectrum. For example, the V-EOG blink artefact has a classic low-frequency response that can be attenuated with by removing correlated ICA components. However, eye blinks are also associated with relatively prolonged changes in alpha and beta power (Liu et al., 2020). In the context of this paper, we consider this to be an 'indirect' artefact; it is spatially and spectrally separated from the artefact source and is unlikely to have arisen from volume conduction. The GLM-Spectrum can detect these differences and remove their effect from the overall mean. As such, it could not have been detected or removed by ICA de-noising. In another context, this might form the contrast of interest, but in this case, we apply confound regression to minimises the effect of eye movements and blinks on the eyes open > eyes closed condition contrast.

## 4.3 Limitations of the GLM-Spectrum model

As outlined in the main text, the parameters of a model are only valid if the underlying assumptions are met. The GLM has several relevant assumptions for the spectrum analysis presented here, particularly at the first level. In particular, the GLM assumes that the residuals of the model are independently and identically distributed. The presence of any temporal autocorrelation in the residuals indicates that this assumption has been violated and the parameter estimates must be interpreted with caution. Future work can account for this shortcoming by building on similar work in fMRI.

The covariate and confound regressors in a GLM-Spectrum model dynamics over time in a highly simplified sense. This approach is appropriate to quantify relatively slow dynamics, on timescales of seconds, in the context of a spectrum estimator that already utilises sliding time segments for spectrum estimation. The sliding windows are tuned for spectral resolution. They have fixed and arbitrary length and may not accurately reflect the true timescale of dynamics in the covariate variables. As such, limited conclusions about underlying dynamics can be made from a GLM-Spectrum.

We can only say that a dynamic relationship existed at the specific timescale selected for spectrum estimation. If precise temporal dynamics are of interest, a more advanced, window-free method such as the Hidden Markov Model (Quinn et al., 2019, 2018; Vidaurre et al., 2018, 2016) or Empirical Mode Decomposition (Huang et al., 1998) might be more appropriate.

## 4.4 Conclusion

The GLM-Spectrum builds on methodologies that are all well established in the field. The novelty of this work is to bring modern statistics and classical spectrum estimation together into a single framework and to thoroughly explore the theoretical, computational, and practical challenges in its use. The result is an approach for spectrum analysis across the whole head and frequency range with the flexibility to generalise to a huge variety of research and engineering questions.

# 5 Funding & Acknowledgments

This project was supported by the Medical Research Council (RG94383/RG89702) and by the NIHR Oxford Health Biomedical Research Centre. The Wellcome Centre for Integrative Neuroimaging is supported by core funding from the Wellcome Trust (203139/Z/16/Z). A.C.N. is supported by the Wellcome Trust (104571/Z/14/Z) and James S. McDonnell Foundation (220020448). M.W.W. is supported by the Wellcome Trust (106183/Z/14/Z; 215573/Z/19/Z). A.C.N. and M.W.W. are further supported by an EU European Training Network grant (euSSN; 860563). This research was funded in whole, or in part, by the Wellcome Trust . For the purpose of open access, the author has applied a CC BY public copyright licence to any Author Accepted Manuscript version arising from this submission.

The computations described in this paper were performed using the University of Birmingham's BlueBEAR HPC service, which provides a High Performance Computing service to the University's research community. See `http://www.birmingham.ac.uk/bear` for more details.

# 6 Author Contributions

AQ: Conceptualization, Methodology, Software, Formal analysis, Data Curation, Project administration, Writing - Original Draft, Writing - Review & Editing, Visualization. LA: Conceptualization, Methodology, Writing - Review & Editing. CG: Conceptualization, Methodology, Writing - Review & Editing. OK: Methodology, Writing - Review & Editing. JP: Formal analysis, Writing - Review & Editing. CZ: Formal analysis, Writing - Review & Editing. ACN: Writing - Review & Editing, Supervision. MWW: Conceptualization, Methodology, Writing - Original Draft, Writing - Review & Editing, Supervision.

# 7 Supporting information

## 7.1 STFT Data Distributions

The general linear model used here expects the dependant variable (the time-varying spectrum) and residuals to follow a Gaussian distribution. Whilst small deviations are permissible, the model fit and any subsequent statistics may be invalid if either is strongly non-Gaussian. This is a concern for the GLM-Spectrum as power values in a standard PSD tend to be non-Gaussian; they are strictly positive and squared (see equation 7). Figure 11A shows an example power spectrum for a single example subject. The second column shows a strongly skewed distribution of power values over time-segments for a single channel and frequency. This skew persists into the distribution of residuals as well, indicating that the model assumptions are likely to be violated for when using PSD estimates as the dependant variable in a GLM.

In this paper, we fix this violation by using the magnitude spectrum rather than the power spectrum. Whilst the magnitude spectrum is less commonly used and has less clear mathematical properties [7], though the distribution of magnitude estimates is more Gaussian than for power estimates. Figure 11B shows an example magnitude spectrum, its data distribution and its residual distribution. All are better distributed than the PSD example in Figure 11A. Another option would have been to use the log-power spectrum, which also has a well-behaved Gaussian distribution Figure 11C.

Here, we restored the GLM model assumptions through a data-transform however a more general solution could be to use a model that is robust to different data and residual distributions. Future work could explore using a Generalised Linear Model which can describe skewed power distributions with an appropriate link function (Nelder and Wedderburn, 1972).

[7] the relation between the sum-square of the time-domain data and the integral of the spectrum does not hold for a magnitude spectrum.

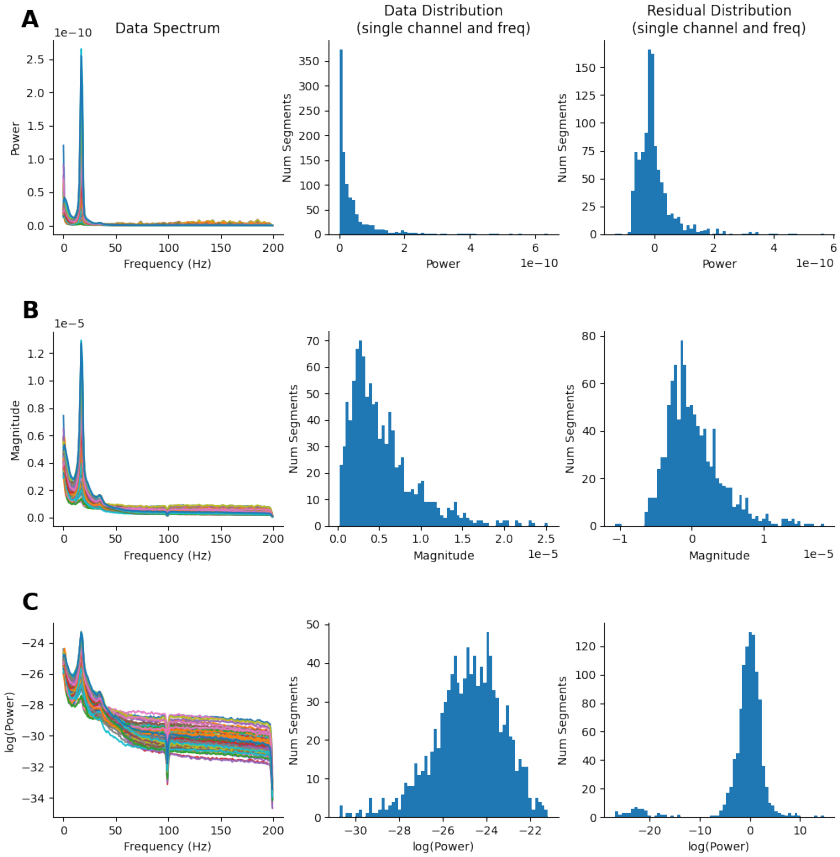


**Fig 11. Distribution of the magnitude, power and log-power spectra for an example dataset.**
**A:** The power spectrum across frequency and channels, the distribution of power values over time-segments and the distribution of residuals after fitting a GLM-Spectrum **B:** As A, for the magnitude spectrum. The data and residual distributions are substantially more Gaussian in shape. **C:** As A for the log-power spectrum. The data and residual distributions are more Gaussian than the power and magnitude spectra.

## 7.2 Parameter settings and resolution in periodograms

When estimating power spectra with a time-averaged approach such as Welch's Method, three parameters are of particular interest: the sampling rate, the length of the window in which the data will be divided, and the length of the data. Changing these parameters can affect the resolution of the spectrum and how many segments are included in the average.

**Segment Length.** The length of the time segments that the data is divided into influences the resolution of the underlying FFT result. In general, more frequencies are estimated from longer time segments. So, increasing window length whilst holding other parameters constant will result in a larger number of frequency bins in the final spectrum estimate. The resolution in Hz can be computed by dividing the segment length by the sample rate of the data

$$\delta f = \frac{N}{fs} \tag{22}$$

For example, a time series with 512 data points sampled at 128Hz would have a frequency resolution of 4Hz. Similarly, the lowest frequencies that can be reliably extracted from the time-series are also dependent of the window length. Frequencies that are slower than the window period cannot be extracted. In general, it is recommended to estimate power of an oscillatory signal across several cycles to reduce the signal-to-noise ratio of the estimation (Cohen, 2014). Therefore, increasing the window size will also allow to assess lower frequencies more reliably (Figure 12A).

There is an additional subtly in some implementations of the FFT that means that the data length does not necessarily equal the length of the computed FFT. For example, the scipy implementation of Welch's method contains parameters for segment length (nperseg) and FFT length (nfft). These are assigned equivalent values by default, but if they are different then the nfft parameter should be used instead of N to compute the frequency resolution.

**Sampling Rate.** The FFT returns estimates at equally spaced frequencies from 0Hz to one half of the sampling rate of the data Nyquist Frequency. The 0Hz component is known as a 'direct current' or DC offset and contains the average of all samples in the segment being analysed. The Nyquist frequency is the fastest observable frequency in the dataset and is one half of the sample rate. As such, increases in the sampling rate, whilst holding other parameters constant, will in result in larger frequency spacing and a lower resolution (Figure 12A). The reason for this is that the same number of frequency bins must cover a larger frequency range. In reverse, this means that decreasing the sampling rate while holding the window length constant results in a smaller frequency spacing and higher spectral resolution.

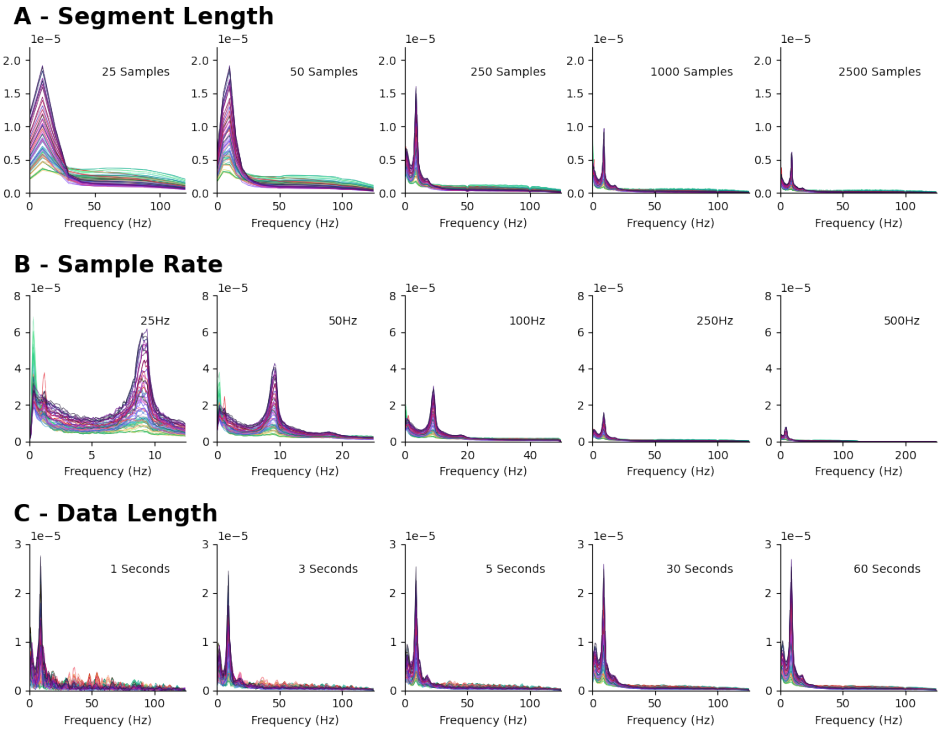


**Fig 12. Influence of parameter choice on time-averaged spectrum estimates.** **A:** The effect of increasing segment length on the spectrum estimate. Longer segment lengths have a higher frequency resolution. **B:** The effect of increasing sample rate on the spectrum estimate. Faster sample rates have higher Nyquist frequencies and lower frequency resolution. **C:** The effect on increasing the length of the analysed data set. Longer datasets have more segments contributing to the central average and are less affected by noise.

Importantly, increasing the frequency spacing is not always better because smaller bins might result in a noisier estimation of the power spectrum (Figure 12B). Small variations in the (intrinsic) frequency of the oscillatory signals - that are in most cases not of particular interest - might be represented by power in various of these small frequency bins whereas larger frequency bins allow to smooth across these smaller, less relevant variations. This results in a smoother power spectrum.

**Length of the overall time-series.** The length of the data determines the number of windows in which the time course is divided by Welch's Method before averaging across power spectra. A higher number of windows results in averaging across a larger number of power spectra which in turn results in a better signal-to-noise ratio of the overall power estimation (Figure 12C). In general, considering more data is preferable because the average of a larger number of window-power spectra should result in an estimation closer to the true average power spectrum according to the law of large numbers. Importantly, dynamic fluctuations in oscillatory power over the time course might introduce meaningful variations in the mean power spectrum that cannot be accounted for by Welch's Method and result in more complex, and less peaky power spectra.

## 7.3 Residual autocorrelation & first-level statistics

In addition to having a Gaussian distribution (see methods section 2.4 and supplemental section 7.1), the residuals of a GLM should also not show any autocorrelation. This is vital concern for the GLM-Spectrum is first-level statistical inference are critical. We do not perform statistical inference at the first-level in this paper due to concerns about validity for this reason. Despite this, it is worth exploring how the choice of parameters in the time-varying spectrum can affect residual auto-correlation in the GLM-Spectrum. Here, we use the Durbin-Watson statistic (Durbin and Watson, 1950, 1951) as a measure of residual autocorrelation for a set of GLM-Spectra fitted on a single dataset. A Durbin-Watson statistic of 2 indicates no autocorrelation, whilst values closer to 0 or 4 indicate the presence of positive and negative autocorrelation respectively.

We computed the Durbin-Watson statistic with the standard first-level design used in this paper for 4 different segment lengths and 3 different window overlaps. Some positive residual autocorrelation exists for the shortest window with an overlap of one sample (Figure 13A; nperseg: 100, nstep: 99) though this drastically reduces for the longer segment lengths in that row. Segment lengths of 500 or 1250 samples show little residual autocorrelation in most channels and frequencies. In contrast, time-varying spectra with longer window overlaps show substantial positive autocorrelation in the residuals for all window lengths (Figure 13B & C). This positive autocorrelation indicates that consecutive segments are likely to have similar residuals. This is strongest in the shortest segment with the largest overlap (Figure 13C; nperseg: 100, nstep: 25) which shows Durbin-Watson statistics close to 0 for most channels and frequencies.

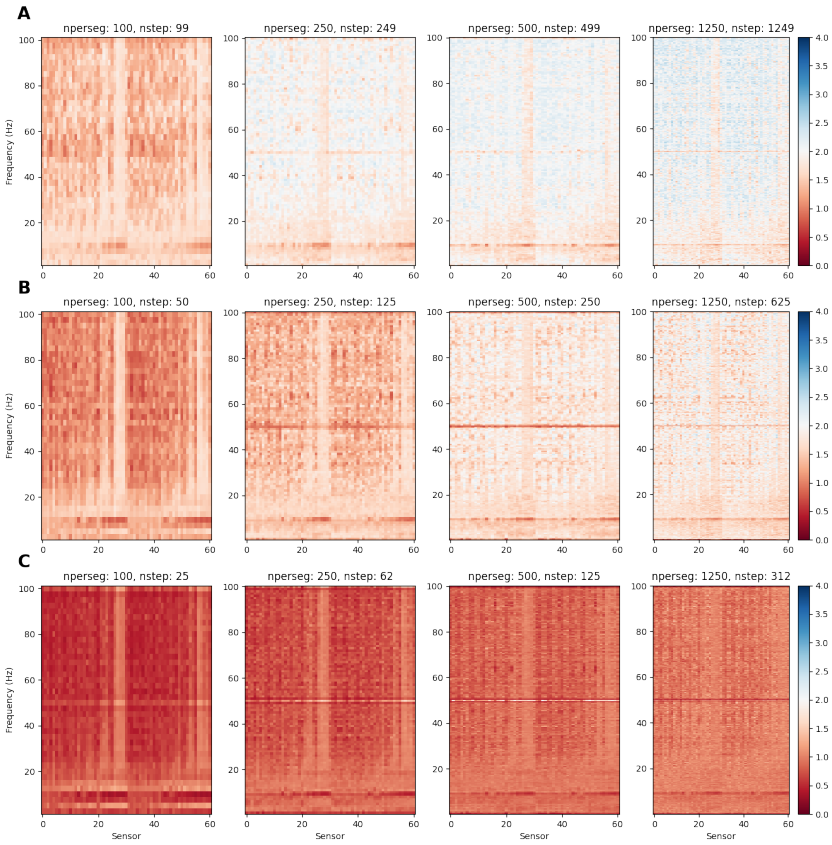


**Fig 13. Durbin-Watson statistics for a GLM-Spectra across a range of segment lengths and step sizes.** Values close to 2 are considered to have no residual autocorrelation indicating a valid GLM fit. Values close to 0 or 4 indicate substantial residual autocorrelation indicating that the assumptions of the GLM have been violated. Several sets of parameters clearly violate the residual autocorrelation assumptions of the GLM, though this can be attenuated by choosing longer segment lengths with a lower overlap.
**A:** The Durbin-Watson values for a range of segment lengths with a single sample overlap between windows. **B:** The Durbin-Watson values for a range of segment lengths with a 50% overlap between windows. **C:** The Durbin-Watson values for a range of segment lengths with a 75% overlap between windows.

## 7.4 Fast standard-error estimation with Einstein summation

The slowest computation in the GLM-Spectrum is obtaining the standard error of the parameter estimates, known as varcopes. This involves large matrix multiplications that are typically repeated across many tests. However, only the diagonal output is used in the eventual varcope estimate. Standard computing approaches will evaluate every single cell within these matrices even though majority contribute to the off-diagonals and are eventually discarded. This is not a large computational expense for single tests but quickly becomes prohibitive when computing large numbers of test together in matrix form. We use the numpy implementation of Einstein summation conventions (Numpy.Einsum — NumPy v1.23 Manual, n.d.)(https://numpy.org/doc/stable/reference/generated/numpy.einsum.html) to compute the most efficient computational path for the varcope evaluation. In practice, this avoids carrying out intermediate multiplications which would eventually be dropped when extracting the diagonal at the final step. The code for the standard 'DotDiag' approach and the new Einsum approache is as follows:

```
resid_var = np.diag(resid.T.dot(resid))  # Standard approach
resid_var = np.einsum('ij,ji->i', resid.T, resid)  # Einsum approach
```

We explore the difference this makes to computation time by running 100 simulated GLMs with each method for each of four datasets. The first dataset was a single GLM that might represent a single channel and frequency bin. The second is a full GLM-Spectrum across 100 frequency bins whilst the third and fourth were GLM-Spectra across 60 or 204 channels, representing common EEG and MEG data sizes. The GLM was computed 100 times for each case and the results are summarised in Figure 14. The computation was equally fast for both methods in the single-test case but the einsum approach can lead to a 1000x speed up in computation time in the larger datasets. This is convenient for in any case but is essential for making non-parametric permutation statistics of GLM-spectra practically feasible.

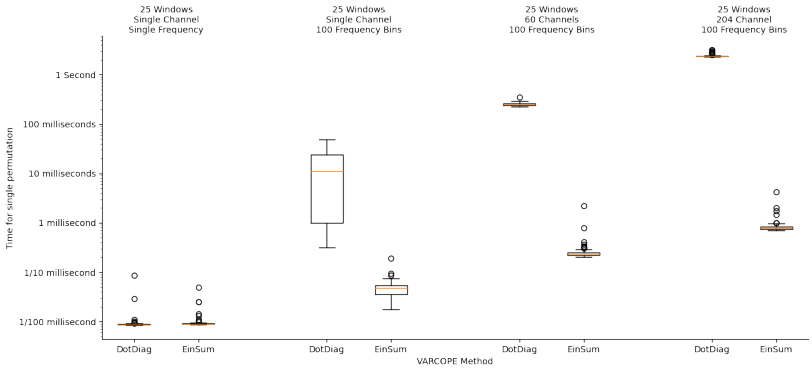


**Fig 14. Computation times for varcope estimation across different data sizes with a standard or einsum based method.** Each data size and method was computed for random data 100 times and the distribution of its timing shows as a boxplot.

## 7.5 Pseudo t Statistics

A standard t-statistic is computed a change divided by the square root of the estimated variance of that change (Nichols and Holmes, 2001). The variance in the denominator of the t-statistic can be estimated poorly, for instance if there are few available degrees of freedom available in the model. In addition, estimates of variance tend to scale in proportion with real effects in the data, reducing the prominence of larger changes. One solution to these issues is the pseudo t-statistic (Nichols and Holmes, 2001).

Figure 15A and B show the cope- and varcope-spectra for the first-level eyes open > eyes closed contrast for an example dataset. The clear negative effect in the low frequencies, peaking around the alpha range is clearly visible in the cope-spectrum, yet is greatly reduced in the corresponding t-spectrum in Figure 15C. This is due to a strong correlation between the cope and varcope estimates in the model Figure 15D). In other words, the square root of the standard error of the contrast value is scaling closely with the contrast value itself. We can assume that the variance structure underlying a spectral effect is relatively smooth over frequency and compute a smoothed varcope-spectrum using a median-filter (Figure 15E). A pseudo t-statistic (Figure 15F) computed with the smoothed varcope values now more closely reflects the effects seen in the original cope-spectrum (Figure 15A).

Note that the distribution of pseudo t-statistic values is not known, so standard parametric statistics are inappropriate (Nichols and Holmes, 2001). However, if the same variance smoothing approach is take across all permutations in a non-parametric statistical approach then the resulting statistics are valid. Any bias created by the smoothing procedure will apply equally to both the observed data and the nulls.

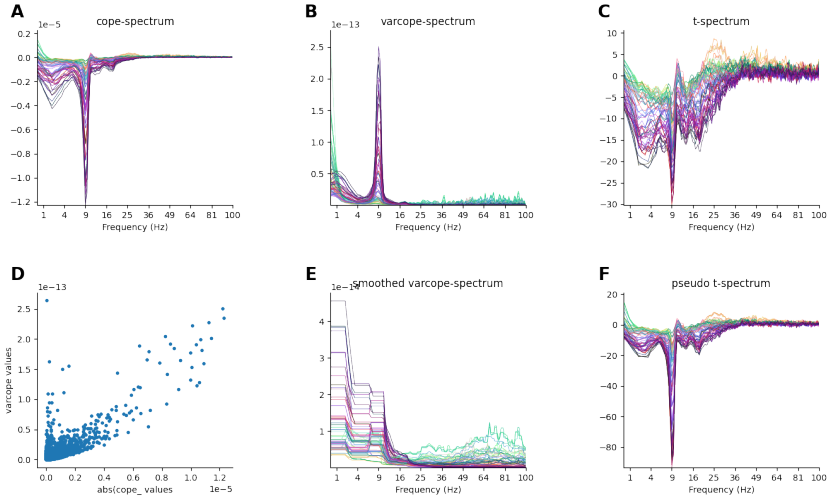


**Fig 15. Illustration of the pseudo t-spectrum computation. Spectra are shown from an example single data recording. A:** An example cope-spectrum **B:** An example varcope-spectrum **C:** Correlation between the cope and varcope values showing a strong positive trend. **D:** The standard t-spectrum for the example dataset. The correlation between the cope and varcope values flattens the observed effects in the cope-spectrum. **E:** A 15-point median filter smoothed varcope spectrum **F:** A pseudo t-spectrum computed from the cope-spectrum and smoothed varcope-spectrum. This better reflects the structure observed in the original cope-spectrum.

## 7.6 Confound Regression

Figure 16A shows an example design matrix for this case. The first regressor is a constant vector of ones and a second regressor tracks the time segments in which the artefact occurs. In isolation, the constant regressor models the data mean (including the time periods that the artefact occurs), but this changes when it is alongside a regressor with non-zero mean in the same model. The constant regressor now models the intercept; this is the expected value of the data when the artefact regressor is zero (Figure 16B – contrast 1 'Intercept'). In turn, the artefact regressor can be interpreted as the difference between the value of the intercept and the mean of the segments indicated in the artefact regressor (Figure 16B – contrast 2 'Artefact Effect'). We can recover the mean of the artefact segments by summing the parameter estimates for both regressors (Figure 16B – contrast 3 'Artefact Mean').

To illustrate the quantities estimated by the simple model and the confound regression, we generate a simulation of 128 data points centred around a 'true' mean of 1 with a small number of outliers centred around 4 (Figure 16C). The simple mean estimated by the 'mean-only' design is biased towards the outlier observations. In contrast, the confound regression quantifies the 'true mean' of 1 in the intercept term as the artefact regressor describes the effect of the artefact. In a real data example, this design could describe the mean spectrum of a resting-state EEG recording whilst accounting for a set of 'bad segments' annotations identified during pre-processing. This both provides an estimate of any 'artefact effect' and linearly removes its influence from the estimate of the mean term.

We can also specify artefact regressor with the mean removed, i.e. with zero means. Counter-intuitively, the interpretation of the regression parameter estimate is unchanged; whereas the interpretation of the constant regressor changes from modelling the intercept (as in Figure 16B) to modelling the mean over all time points.

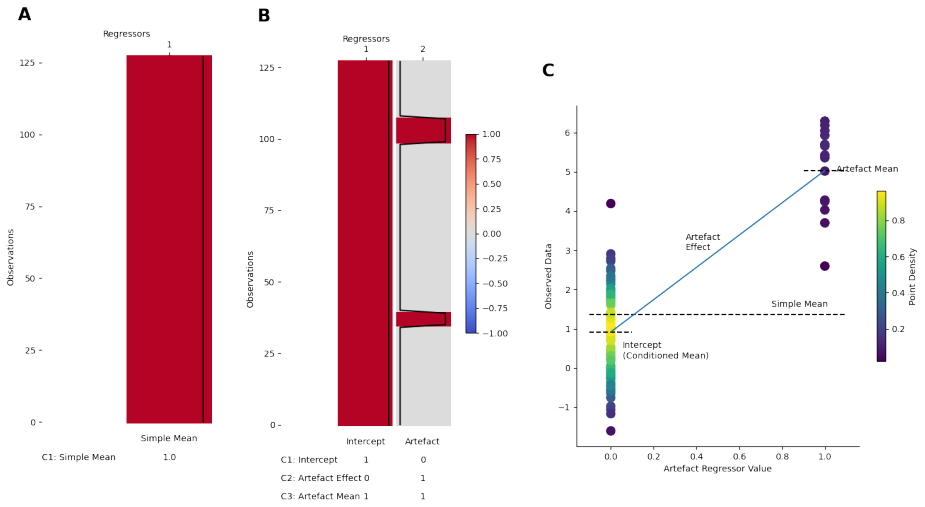


**Fig 16. GLM-Spectrum design matrix for confound regression. A:** A GLM design with a single regressor and contrast modelling a simple mean of the observed data **B:** A GLM design with two regressors and three contrasts illustrating confound regression. The first regressor is a constant term and the second is a sparse, non-zero mean artefact regressor indicating data observations that are possible artefacts. Three contrasts isolate each regressor individually (intercept and artefact effect) and their sum (artefact mean). **C:** Simulated data observations and the quantities estimated by the GLM designs in A and B. The first design estimates the simple mean overall data, though this is heavily influenced by the possible outlier points. The second design models an intercept and an artefact effect. The intercept can be thought of as the mean where the artefact regressor equals zero, and the artefact effect is the distance between the intercept and the artefact mean. Finally, the absolute artefact mean can be reconstructed by the sum of the two parameter estimates as shown in B contrast 3.

# References


Adrian, E. D. and Matthews, B. H. C. (1934). The berger rhythm: Potential change from the occpital lobes in man. *Brain*, 57(4):355–385.

Akaike, H. (1974). A new look at the statistical model identification. *IEEE Transactions on Automatic Control*, 19(6):716–723.

Aurlien, H., Gjerde, I. O., Aarseth, J. H., Eldøen, G., Karlsen, B., Skeidsvoll, H., and Gilhus, N. E. (2004). EEG background activity described by a large computerized database. *Clinical Neurophysiology*, 115(3):665–673.

Babayan, A., Erbey, M., Kumral, D., Reinelt, J. D., Reiter, A. M. F., Röbbig, J., Schaare, H. L., Uhlig, M., Anwander, A., Bazin, P.-L., Horstmann, A., Lampe, L., Nikulin, V. V., Okon-Singer, H., Preusser, S., Pampel, A., Rohr, C. S., Sacher, J., Thöne-Otto, A., Trapp, S., Nierhaus, T., Altmann, D., Arelin, K., Blöchl, M., Bongartz, E., Breig, P., Cesnaite, E., Chen, S., Cozatl, R., Czerwonatis, S., Dambrauskaite, G., Dreyer, M., Enders, J., Engelhardt, M., Fischer, M. M., Forschack, N., Golchert, J., Golz, L., Guran, C. A., Hedrich, S., Hentschel, N., Hoffmann, D. I., Huntenburg, J. M., Jost, R., Kosatschek, A., Kunzendorf, S., Lammers, H., Lauckner, M. E., Mahjoory, K., Kanaan, A. S., Mendes, N., Menger, R., Morino, E., Näthe, K., Neubauer, J., Noyan, H., Oligschläger, S., Panczyszyn-Trzewik, P., Poehlchen, D., Putzke, N., Roski, S., Schaller, M.-C., Schieferbein, A., Schlaak, B., Schmidt, R., Gorgolewski, K. J., Schmidt, H. M., Schrimpf, A., Stasch, S., Voss, M., Wiedemann, A., Margulies, D. S., Gaebler, M., and Villringer, A. (2019). A mind-brain-body dataset of MRI, EEG, cognition, emotion, and peripheral physiology in young and old adults. *Scientific Data*, 6(1).

Babiloni, C., Lizio, R., Vecchio, F., Frisoni, G. B., Pievani, M., Geroldi, C., Claudia, F., Ferri, R., Lanuzza, B., and Rossini, P. M. (2011). Reactivity of cortical alpha rhythms to eye opening in mild cognitive impairment and alzheimer's disease: an EEG study. *Journal of Alzheimer's Disease*, 22(4):1047–1064.

Baker, D. H. (2021). Statistical analysis of periodic data in neuroscience. *Neurons, Behavior, Data analysis, and Theory*, 5(3).

Bartlett, M. S. (1948). Smoothing periodograms from time-series with continuous spectra. *Nature*, 161(4096):686–687.

Bartlett, M. S. (1950). Perioidogram analysis and continuous spectra. *Biometrika*, 37(1-2):1–16.

Beckmann, C. F., Jenkinson, M., and Smith, S. M. (2003). General multilevel linear modeling for group analysis in FMRI. *NeuroImage*, 20(2):1052–1063.

Buzsaḱi, G. and Draguhn, A. (2004). Neuronal oscillations in cortical networks. *Science*, 304(5679):1926–1929.

Cohen, M. X. (2014). *Analyzing Neural Time Series Data*. The MIT Press.

Cooley, J. W. and Tukey, J. W. (1965). An algorithm for the machine calculation of complex fourier series. *Mathematics of Computation*, 19(90):297–301.

Durbin, J. and Watson, G. S. (1950). Testing for serial correlation in least squares regression. i. *Biometrika*, 37(3-4):409–428.

Durbin, J. and Watson, G. S. (1951). Testing for serial correlation in least squares regression. ii. *Biometrika*, 38(1-2):159–178.

Friston, K., Josephs, O., Zarahn, E., Holmes, A., Rouquette, S., and Poline, J.-B. (2000). To smooth or not to smooth? *NeuroImage*, 12(2):196–208.

Friston, K., Penny, W., Phillips, C., Kiebel, S., Hinton, G., and Ashburner, J. (2002). Classical and bayesian inference in neuroimaging: Theory. *NeuroImage*, 16(2):465–483.

Friston, K. J., editor (2007). *Statistical parametric mapping: the analysis of funtional brain images*. Elsevier/Academic Press, Amsterdam ; Boston, 1st ed edition.

Friston, K. J., Holmes, A. P., Worsley, K. J., Poline, J.-P., Frith, C. D., and Frackowiak, R. S. J. (1994). Statistical parametric maps in functional imaging: A general linear approach. *Human Brain Mapping*, 2(4):189–210.

Gohil, C., Roberts, E., Timms, R., Skates, A., Higgins, C., Quinn, A., Pervaiz, U., van Amersfoort, J., Notin, P., Gal, Y., Adaszewski, S., and Woolrich, M. (2022). Mixtures of large-scale dynamic functional brain network modes. *NeuroImage*, 263:119595.

Gramfort, A. (2013). MEG and EEG data analysis with MNE-python. *Frontiers in Neuroscience*, 7.

Greve, D. N. and Fischl, B. (2009). Accurate and robust brain image alignment using boundary-based registration. *NeuroImage*, 48(1):63–72.

Harris, C. R., Millman, K. J., van der Walt, S. J., Gommers, R., Virtanen, P., Cournapeau, D., Wieser, E., Taylor, J., Berg, S., Smith, N. J., Kern, R., Picus, M., Hoyer, S., van Kerkwijk, M. H., Brett, M., Haldane, A., del Río, J. F., Wiebe, M., Peterson, P., Gérard-Marchant, P., Sheppard, K., Reddy, T., Weckesser, W., Abbasi, H., Gohlke, C., and Oliphant, T. E. (2020). Array programming with NumPy. *Nature*, 585(7825):357–362.

Huang, N. E., Shen, Z., Long, S. R., Wu, M. C., Shih, H. H., Zheng, Q., Yen, N.-C., Tung, C. C., and Liu, H. H. (1998). The empirical mode decomposition and the hilbert spectrum for nonlinear and non-stationary time series analysis. *Proceedings of the Royal Society of London. Series A: Mathematical, Physical and Engineering Sciences*, 454(1971):903–995.

Hunter, J. D. (2007). Matplotlib: A 2d graphics environment. *Computing in Science and Engineering*, 9(3):90–95.

Hyvarinen, A. (1999). Fast and robust fixed-point algorithms for independent component analysis. *IEEE Transactions on Neural Networks*, 10(3):626–634.

Jenkinson, M., Bannister, P., Brady, M., and Smith, S. (2002). Improved optimization for the robust and accurate linear registration and motion correction of brain images. *NeuroImage*, 17(2):825–841.

Jenkinson, M. and Smith, S. (2001). A global optimisation method for robust affine registration of brain images. *Medical Image Analysis*, 5(2):143–156.

Kayser, J. and Tenke, C. E. (2015). On the benefits of using surface laplacian (current source density) methodology in electrophysiology. *International Journal of Psychophysiology*, 97(3):171–173.

Klimesch, W. (1999). EEG alpha and theta oscillations reflect cognitive and memory performance: a review and analysis. *Brain Research Reviews*, 29(2-3):169–195.

Kopell, N. J., Gritton, H. J., Whittington, M. A., and Kramer, M. A. (2014). Beyond the connectome: The dynome. *Neuron*, 83(6):1319–1328.

Litvak, V., Jha, A., Flandin, G., and Friston, K. (2013). Convolution models for induced electromagnetic responses. *NeuroImage*, 64:388–398.

Liu, C. C., Hajra, S. G., Pawlowski, G., Fickling, S. D., Song, X., and D'Arcy, R. C. (2020). Differential neural processing of spontaneous blinking under visual and auditory sensory environments: An EEG investigation of blink-related oscillations. *NeuroImage*, 218:116879.

Merkin, A., Sghirripa, S., Graetz, L., Smith, A. E., Hordacre, B., Harris, R., Pitcher, J., Semmler, J., Rogasch, N. C., and Goldsworthy, M. (2022). Do age-related differences in aperiodic neural activity explain differences in resting EEG alpha? *Neurobiology of Aging*.

Monti, M. (2011). Statistical analysis of fMRI time-series: A critical review of the GLM approach. *Frontiers in Human Neuroscience*, 5.

Nelder, J. A. and Wedderburn, R. W. M. (1972). Generalized linear models. *Journal of the Royal Statistical Society. Series A (General)*, 135(3):370.

Nichols, T. E. and Holmes, A. P. (2001). Nonparametric permutation tests for functional neuroimaging: A primer with examples. *Human Brain Mapping*, 15(1):1–25.

Penrose, R. (1956). On best approximate solutions of linear matrix equations. *Mathematical Proceedings of the Cambridge Philosophical Society*, 52(1):17–19.

Perrin, F., Pernier, J., Bertrand, O., and Echallier, J. (1989). Spherical splines for scalp potential and current density mapping. *Electroencephalography and Clinical Neurophysiology*, 72(2):184–187.

Prerau, M. J., Brown, R. E., Bianchi, M. T., Ellenbogen, J. M., and Purdon, P. L. (2017). Sleep neurophysiological dynamics through the lens of multitaper spectral analysis. *Physiology*, 32(1):60–92.

Quinn, A. and Hymers, M. (2020). SAILS: Spectral analysis in linear systems. *Journal of Open Source Software*, 5(47):1982.

Quinn, A. J., van Ede, F., Brookes, M. J., Heideman, S. G., Nowak, M., Seedat, Z. A., Vidaurre, D., Zich, C., Nobre, A. C., and Woolrich, M. W. (2019). Unpacking transient event dynamics in electrophysiological power spectra. *Brain Topography*, 32(6):1020–1034.

Quinn, A. J., van Es, M., Gohil, C., and Woolrich, M. W. (2022). Ohba software library in python (osl). `https://zenodo.org/record/6875060`.

Quinn, A. J., Vidaurre, D., Abeysuriya, R., Becker, R., Nobre, A. C., and Woolrich, M. W. (2018). Task-evoked dynamic network analysis through hidden markov modeling. *Frontiers in Neuroscience*, 12.

Rosner, B. (1983). Percentage points for a generalized ESD many-outlier procedure. *Technometrics*, 25(2):165–172.

Smith, N. J. and Kutas, M. (2014). Regression-based estimation of ERP waveforms: I. the rERP framework. *Psychophysiology*, 52(2):157–168.

Smith, S., Jenkinson, M., Beckmann, C., Miller, K., and Woolrich, M. (2007). Meaningful design and contrast estimability in FMRI. *NeuroImage*, 34(1):127–136.

Smith, S. M. (2002). Fast robust automated brain extraction. *Human Brain Mapping*, 17(3):143–155.

Stone, M. (1974). Cross-validatory choice and assessment of statistical predictions. *Journal of the Royal Statistical Society: Series B (Methodological)*, 36(2):111–133.

Thomson, D. (1982). Spectrum estimation and harmonic analysis. *Proceedings of the IEEE*, 70(9):1055–1096.

Vidaurre, D., Hunt, L. T., Quinn, A. J., Hunt, B. A. E., Brookes, M. J., Nobre, A. C., and Woolrich, M. W. (2018). Spontaneous cortical activity transiently organises into frequency specific phase-coupling networks. *Nature Communications*, 9(1).

Vidaurre, D., Quinn, A. J., Baker, A. P., Dupret, D., Tejero-Cantero, A., and Woolrich, M. W. (2016). Spectrally resolved fast transient brain states in electrophysiological data. *NeuroImage*, 126:81–95.

Virtanen, P., Gommers, R., Oliphant, T. E., Haberland, M., Reddy, T., Cournapeau, D., Burovski, E., Peterson, P., Weckesser, W., Bright, J., van der Walt, S. J., Brett, M., Wilson, J., Millman, K. J., Mayorov, N., Nelson, A. R. J., Jones, E., Kern, R., Larson, E., Carey, C. J., Polat, İ., Feng, Y., Moore, E. W., VanderPlas, J., Laxalde, D., Perktold, J., Cimrman, R., Henriksen, I., Quintero, E. A., Harris, C. R., Archibald, A. M., Ribeiro, A. H., Pedregosa, F., van Mulbregt, P., Vijaykumar, A., Bardelli, A. P., Rothberg, A., Hilboll, A., Kloeckner, A., Scopatz, A., Lee, A., Rokem, A., Woods, C. N., Fulton, C., Masson, C., Häggström, C., Fitzgerald, C., Nicholson, D. A., Hagen, D. R., Pasechnik, D. V., Olivetti, E., Martin, E., Wieser, E., Silva, F., Lenders, F., Wilhelm, F., Young, G., Price, G. A., Ingold, G.-L., Allen, G. E., Lee, G. R., Audren, H., Probst, I., Dietrich, J. P., Silterra, J., Webber, J. T., Slavič, J., Nothman, J., Buchner, J., Kulick, J., Schönberger, J. L., de Miranda Cardoso, J. V., Reimer, J., Harrington, J., Rodríguez, J. L. C., Nunez-Iglesias, J., Kuczynski, J., Tritz, K., Thoma, M., Newville, M., Kümmerer, M., Bolingbroke, M., Tartre, M., Pak, M., Smith, N. J., Nowaczyk, N., Shebanov, N., Pavlyk, O., Brodtkorb, P. A., Lee, P., McGibbon, R. T., Feldbauer, R., Lewis, S., Tygier, S., Sievert, S., Vigna, S., Peterson, S., More, S., Pudlik, T., Oshima, T., Pingel, T. J., Robitaille, T. P., Spura, T., Jones, T. R., Cera, T., Leslie, T., Zito, T., Krauss, T., Upadhyay, U., Halchenko, Y. O., and and, Y. V.-B. (2020). SciPy 1.0: fundamental algorithms for scientific computing in python. *Nature Methods*, 17(3):261–272.

Voytek, B., Kramer, M. A., Case, J., Lepage, K. Q., Tempesta, Z. R., Knight, R. T., and Gazzaley, A. (2015). Age-Related Changes in 1/f Neural Electrophysiological Noise. *Journal of Neuroscience*, 35(38):13257–13265.

Wan, L., Huang, H., Schwab, N., Tanner, J., Rajan, A., Lam, N. B., Zaborszky, L., shan R. Li, C., Price, C. C., and Ding, M. (2018). From eyes-closed to eyes-open: Role of cholinergic projections in EC-to-EO alpha reactivity revealed by combining EEG and MRI. *Human Brain Mapping*, 40(2):566–577.

Welch, P. (1967). The use of fast fourier transform for the estimation of power spectra: A method based on time averaging over short, modified periodograms. *IEEE Transactions on Audio and Electroacoustics*, 15(2):70–73.

Winkler, A. M., Ridgway, G. R., Webster, M. A., Smith, S. M., and Nichols, T. E. (2014). Permutation inference for the general linear model. *NeuroImage*, 92:381–397.

Woolrich, M. W., Behrens, T. E., Beckmann, C. F., Jenkinson, M., and Smith, S. M. (2004). Multilevel linear modelling for FMRI group analysis using bayesian inference. *NeuroImage*, 21(4):1732–1747.

Woolrich, M. W., Jbabdi, S., Patenaude, B., Chappell, M., Makni, S., Behrens, T., Beckmann, C., Jenkinson, M., and Smith, S. M. (2009). Bayesian analysis of neuroimaging data in FSL. *NeuroImage*, 45(1):S173–S186.

Woolrich, M. W., Ripley, B. D., Brady, M., and Smith, S. M. (2001). Temporal autocorrelation in univariate linear modeling of FMRI data. *NeuroImage*, 14(6):1370–1386.

Worsley, K. and Friston, K. (1995). Analysis of fMRI time-series revisited—again. *NeuroImage*, 2(3):173–181.

Xifra-Porxas, A., Niso, G., Larivière, S., Kassinopoulos, M., Baillet, S., Mitsis, G. D., and Boudrias, M.-H. (2019). Older adults exhibit a more pronounced modulation of beta oscillations when performing sustained and dynamic handgrips. *NeuroImage*, 201:116037.

Zhang, Y., Brady, M., and Smith, S. (2001). Segmentation of brain MR images through a hidden markov random field model and the expectation-maximization algorithm. *IEEE Transactions on Medical Imaging*, 20(1):45–57.

Zibrandtsen, I. C. and Kjaer, T. W. (2021). Fully automatic peak frequency estimation of the posterior dominant rhythm in a large retrospective hospital EEG cohort. *Clinical Neurophysiology Practice*, 6:1–9.